FINAL 2015 5794

Project Title: Prototype Development and Evaluation of Self-Cleaning Concentrated Solar Power Collectors

Project Period: August 1, 2012 to January 31, 2015

Submission Date: March 31, 2015

Prime Recipient: Boston University, 881 Commonwealth Ave. Boston, MA 02215

Award Number: DOE DE-EE0005794

Sub-Recipient: Abengoa Solar Inc., 11500 W. 13th St. Lakewood, Co 80215

Sub-Recipient: Sandia National laboratory, P.O. Box 5800, MS-1127, Albuquerque, NM 87185

Working Partners: Abengoa Solar Inc., Sandia National Lab, Corning, ITRI

Project Team:
Boston university: Faculty: Malay K. Mazumder, Mark N. Horenstein, Nitin Joglekar
Graduate students: Jeremy Stark, Arash Sayyah, Fang Hao*, John Hudelson*, Calvin Heiling*, Kalev Jaakson*, Emre Guzelesu, and Zhongkai Xu*, Daniel Erickson*,
Undergrad students: Steven Jung*, Atri Roy Chowdhury, Daniel Neumann*, Troy Wilson*, Vicente Colmenares*, Matt Beardsworth*, Dave Crowell, Bryan Jimenez, Bill Chaiyasarikul and Hannah Gibson
*Graduated

Abengoa Solar: Adam Bott

Sandia National laboratory: Clifford Ho and Julius Yellowhair

Corning: Sean Garner

ITRI: H. Y. Lin

Principal Investigator: Malay K. Mazumder, Research Professor, Phone: 617 353 0162 (office) 617 997 7049 (Cell), Fax; 617 353 6440, email: mazumder@bu.edu

Technical Manager: Andru Prescod, andru.prescod@ee.doe.gov, Solar Energy Technology Program

Technology Project Officer: Thomas Rueckert, thomas.rueckert@ee.doe.gov, (202) 586-0942

GO Contracting Officer: Kenneth Outlaw, "Outlaw, Kenneth"Kenneth.Outlaw@go.doe.gov, (720) 356 1739, Golden, CO

EXECUTIVE SUMMARY

The feasibility of integrating and retrofitting transparent electrodynamic screens (EDS) on the front surfaces of solar collectors was established as a means to provide active self-cleaning properties for parabolic trough and heliostat reflectors, solar panels, and Fresnel lenses. Prototype EDS-integrated solar collectors, including second-surface glass mirrors, metallized Acrylic-film mirrors, and dielectric mirrors, were produced and tested in environmental test chambers for removing the dust layer deposited on the front surface of the mirrors. The evaluation of the prototype EDS-integrated mirrors was conducted using dust and environmental conditions that simulate the field conditions of the Mojave Desert.

Test results showed that the specular reflectivity of the mirrors could be maintained at over 90% over a wide range of dust loadings ranging from 0 to 10 g/m^2, with particle diameter varying from 1 to 50 μm. The measurement of specular reflectivity (SR) was performed using a D&S Reflectometer at wavelength 660 nm. A non-contact reflectometer was designed and constructed for rapid measurement of specular reflectivity at the same wavelength. The use of this new noncontact instrument allowed us to measure SR before and after EDS activation. Several EDS prototypes were constructed and evaluated with different electrode configurations, electrode materials, and encapsulating dielectric materials.

Similar tests were conducted on EDS-integrated solar panels, the output power was measured by determining the open circuit voltage and the short-circuit current before and after EDS activation. The output power could be restored to more than 95% of the clean-surface efficiency by EDS activation under the same soiling tests. The energy required for removing the dust layer from the solar collectors was less than 0.1 Wh/m^2 per cleaning cycle. More than 90% of the deposited dust was removed within a 2-minute period for each cleaning cycle.

Both theoretical analysis and optical modeling were performed to optimize the electrode geometry and choice of materials of prototype EDS mirrors for restoring specular reflectivity. Optical modeling provided a comparative analysis of (1) the initial loss of SR (ΔR_s) caused by the integration of EDS with (2) the loss of SR due to dust deposition as a function of surface mass concentration. Since loss of reflectance and transmission efficiency by dust deposits depends upon the projected surface area of the particles intercepting the incident and reflected beams, a dust deposition analyzer was designed and constructed to measure the fraction of surface area covered by the dust particles before and after EDS operation. This analyzer was used for measuring dust removal efficiency (DRE). The measurements of ΔR_s and DRE were used to determine the figure of Merit (FOM) of the EDS configuration defined by FOM = DRE/ ΔR_s.

Both theoretical and experimental analyses on the optimization of electrode geometry and the choice of electrode and dielectric materials were studied based on their optical transparency, durability, and electrical properties for achieving maximum value of FOM. The studies showed that application of silver-nanowire ink as an electrode material at 50-μm width, 750-μm inter-electrode spacing, and 1-μm thickness provided the best figure of merit.

Prototype EDS mirrors were constructed by depositing rows of transparent parallel electrodes using a screen-printer. For EDS integration, the electrodes were printed directly on the front surface of the solar collectors (second surface mirrors or on the glass cover plates of solar panels) and were embedded within a transparent dielectric film having a thickness of 50 μm. For retrofitting applications, the electrodes are printed on a flexible transparent dielectric film and then laminated on the surface of the mirrors (or solar panels) using an optically clear adhesive (OCA) film.

Experimental studies were conducted with electrodes made from (1) Indium Tin Oxide (ITO), (2) Chrome, (3) silver paste, (4) silver nanowire (AgNW) ink and (5) and a conducting polymer, PEDOT:PSS [poly(3,4-ethylenedioxythiophene) poly-styrenesulfonate.

The electrodes were deposited on the substrate using either a screen-printer or by photolithography. For dielectric film encapsulation, several dielectric materials were used: (1) urethane, applied using a Meyer rod coating process, (2) UV-stabilized acrylic film or FEP (fluoro-ethylene-propylene) film laminated on the surface via an OCA adhesive film, and (3) ultrathin flexible glass film glass (Corning® Willow® Glass) laminated by OCA film. For EDS integration on the mirrors the electrodes were printed directly on the surface of the glass mirrors. For producing flexible EDS film, the electrode printing is done by either a screen-printer or a gravure offset printer.

Best results were obtained when we used silver nanowire electrodes printed on ultrathin (100-μm thick), flexible glass substrates. A transparent, UV-resistant, fluoropolymer film (FEP) can also be applied on the front side of the glass film to make the surface hydrophobic for reducing dust adhesion. The front surface of the ultrathin, highly transparent, UV radiation resistant Willow® Glass faces the sun that provides provides protection against scratch, abrasion from sand impaction and hail, and moisture ingress.

The flexibility of EDS film makes it suitable for affixing it on the flat or curved surfaces of the solar collectors used in CSP (both parabolic trough, glass envelope of the receiver tube, heliostats), CPV (Fresnel lens and Fresnel mirrors) and PV modules.

Experimental data were taken on dust deposition and restoration of specular-reflection by activating EDS over 100 operation cycles. Original SR of the mirror was 97.1%; after EDS integration, the SR was 94.4% without dust. Reduction in SR as dust was deposited on the mirror's surface was measured. When the loss of reflectivity was approximately 3 to 5% by the deposited dust layer, EDS was operated. Over the 100 cycles of dust deposition and EDS based restoration were conducted, the specular reflectivity could be maintained over 87%. Restored SR was more than 90% of the original value after EDS activation for 1 min/cycle. The total mass of deposited dust represents more than a year of soiling in the Mojave Desert region.

To activate the electrodynamic dust removal process, three-phase, low current, high voltage pulses are applied to the electrodes. The electric field created by the electrodes produces non-uniform, time varying force distributions comprised of Coulomb and dielectrophoretic forces on the EDS surface. The dust particles become electrostatically charged by the electric field induced charge injection to the surface and by the friction of particles undergoing translational and rotational motion on the EDS surface. The charged particles are levitated by the Coulomb force and swept away laterally over the collector surface by the travelling electric field. Each of the power supplies we designed has a maximum power output of 1 W and is capable of delivering the three-phase pulses at frequencies in the range 1 to 200 Hz. Each power supply unit can be operated remotely and can service multiple EDS screens.

The electrodynamic dust removal process was modeled by using Quickfield and COMSOL software programs, and the optical performance of EDS was analyzed by using FRED optical software. The analyses showed that our current EDS design would be capable of removing dust particles in the size range 0.8 to 100 μm. Most of the dust particles that deposit on solar collectors under normal and dust-storm conditions fall within this size range.

EDS cost modeling was performed with two-fold objectives: (1) to assess the economic viability of the EDS technology used in conjunction with solar collecting technologies when it is put in place into large scale EDS operations, and (2) to help make informed development decisions as the EDS technology matures in the lab. This analysis is made up to two modules: (i) Manufacturing costs analysis, and (ii) Integrated cost analysis that incorporated both the manufacturing and operational costs.

Based on this integrated analysis, we developed a levelized cost of mirror cleaning (LCOMC) metric to link the EDS-enhanced reflectivity gains with the relevant product and installation costs, as well as with the direct and indirect costs associated with plant operation and maintenance. For the configuration studied, it is shown that, if the EDS technology production and installation cost is $\$10/m^2$, then its LCOMC is 7.9% below the LCOMC for a comparable deluge cleaning alternative. Thus, the proposed LCOMC metric provides a methodology for

systemic assessment of the economic impact of the EDS technology (and other mirror cleaning technologies), early in its technology development cycle.

Throughout the project, we worked with Sandia National Laboratory (SNL) and Abengoa Solar. During the project we also collaborated with BrightSource, Corning, and Industrial Technology Research Institute (ITRI). The collaboration would allow us to develop a technology roadmap for extensive field-testing of the prototype EDS in the Ivanpah plant site at the Mojave Desert, Dimona Plant site in Israel, and in CSP and Solar Module plan sites at the Atacama Desert in Chile. We received samples of EDS film with Ag-paste electrodes printed on ultrathin glass film produced by the gravure offset printing process. The experimental data obtained from the prototype EDS produced in production environment agreed with the predicted value from modeling analysis carried out at SNL.

TABLE OF CONTENTS

1. Executive Summary 1
2. Background 8
3. Introduction 10
4. Project Results and discussions 11

1.1 Optical efficiency in CSP systems: 11
1.2 Atmospheric dust deposition: 13
1.3 Size distribution of dust particles in arid and semi-arid areas: 14
1.4 Dust deposition rates in deserts and in semi-arid areas 14
1.5 Power Law distribution and residence time of the particles in the atmosphere: 15
2. Adhesion of dust on the surface of solar collectors: 15

3. Loss of Optical Efficiency Caused by Dust Deposits on Solar Mirrors 16
3.1 Transmission Loss 17
3.2 Reflection Loss 18
3.3 Estimation of Specular Reflection Loss 18

4. Modeling of Loss of Optical Efficiency Caused by Dust Deposition on Solar Collectors 20

5. Energy Required for the Removal of a Deposited Dust Layer 22

6. Prototype Developments and Evaluation of Transparent Electrodynamic Screens: 23
6.1 EDS configuration: 23

7. Construction of prototype EDS mirrors by an integration process: 24
7.1 EDS-integration during the manufacturing process: 25
7.2 EDS film production for retrofitting 25

8. Electrostatic Charging Process in EDS 26
8.1 Experimental Data on Charge-to-Mass Ratio 29

9. EDS Design Parameters and Construction Features 30
9.1 Optimization of EDS Electrode Geometry and Material 31
9.2 Figure of Merit 31
9.3 Summary of Electrode Deposition Processes 35
9.4 Dielectric film 35
9.5 Optimization of EDS Electrode Geometry for High Specular Reflectivity and Dust Removal Efficiency 36

10. Specular Reflectivity Restoration by EDS Operation for Removing Deposited Dust from the Mirrors 37
10.1 Silver nanowire ink electrode with Polymer (PET) film 38
10.2 Silver nanowire ink electrode with ultrathin flexible glass film 41

11. Power Supply Design and Construction 41
11.1 Power Supply Safety Features 42

12. Field Testing at Sandia National Laboratories 42
12.1 Summary of field-testing results 45
12.2 Durability tests for AgNW electrodes 45

13. Prototype EDS mirror development by gravure offset printing with Ag-paste electrodes printed on willow glass at ITRI 45

14. Economic Analysis: EDS Manufacturing & Operations Processes 46
14.1 Manufacturing Cost Analysis 46
14.2 Integrated Cost Analysis Using LCOMC Metric 48
14.3 Baseline LCOMC (with Deluge Cleaning) 48
14.4 LCOMC with EDS 49
14.5 Results 49
14.6 Roadmap 49

CONCLUSIONS: Project Goals Accomplished 50

PATH FPRWARD: Technical roadmap established for manufacturing and field-evaluation 52

REFERENCES 53

BACKGROUND

Semi-arid and desert areas have the solar energy delivery capacity to meet current and future global needs. For example, just the seven largest deserts in the world have the solar power capacity for meeting energy needs permanently, assuming energy storage and distribution technologies become available on the terawatt-hour scale. Solar power plants on the MW and GW scales comprise Photovoltaic (PV) modules, Concentrated Solar Power (CSP) systems, and Concentrated PV (CPV) systems. These installations require vast areas of land having high Direct Normal Irradiance (DNI), however, land must be acquired without competing for it with farming and other industries.

Available solar energy in deserts [1] is highest in the African Sahara Desert (2.7 MWh/m^2/yr), followed by the Chilean Atacama Desert and the Great Sandy Desert of Australia (2.3 MWh/m^2/yr), the Negev Desert of Israel (2.3 MWh/m^2/yr), the Thar Desert of India (2.2 MWh/m^2/yr), the Mojave Desert of the US 2.1 MWh/m^2/yr), and the Gobi Desert in China (1.701 MWh/m^2/yr.) These vast regions have inherently high, reliable solar irradiance with minimal interruption from cloud and rain. However, significant attenuation of solar radiation occurs due to high amounts of (a) atmospheric dust concentration, (b) rates of dust deposition on solar collectors, (c) ambient temperature, (d) wind speed, and (e) relative humidity (RH) in the morning hours (when the area is located near an ocean). Daily cycling of temperature and RH over wide ranges causes corrosion by the combination of dust and high humidity. Efficiency losses are reported [2 – 6] from 10 to 50% for solar plants. Solar plants in these sun-rich areas

have high operation and maintenance (O&M) costs because of the frequent dust cleaning requirements. Lack of rain, absence of large fresh water reservoirs, and high labor cost at the solar fields all increase O&M cost.

For high optical efficiency, the optical surface of a solar collector must be free of any contaminants that can reduce light transmission or reflection. To maintain the reflection efficiency of solar mirrors in CSP plants or the transmission efficiency of PV modules higher than 90%, the solar collectors must be cleaned periodically at a frequency that depends on the rate of dust deposition. Washing solar collectors with water and detergent is the most effective cleaning method for soiling losses. However, manual or robotic cleaning with water is both labor and energy intensive; it is disruptive of routine operation of the plant and is often a critical problem where conservation of water is needed in areas where water is scarce. Methods to maintain clean solar panels and solar concentrators while realizing reduced water consumption or no water use at all is a desirable goal.

Most of the efforts to achieve this goal involved two approaches: (1) passive treatment of the optical surface for reducing adhesion of dust on the collector surface and (2) robotic brush cleaning of the surface. Most of the soil cleaning processes reported earlier involves passive hydrophobic surface treatment methods to modify the front glass cover plates of solar collectors easily cleanable or non-sticky. This method reduces dust adhesion substantially, but water or high wind speed is still needed for cleaning the surface.

Both surface coating and robotic technologies in developmental stages for mitigation of soiling losses. Coating of the front surface materials of solar energy harvesting systems could play an important role in reduction of soiling losses. Appels *et al.* [7] performed an experiment in which coated glass samples were tilted at 35° and exposed for three weeks to the outdoor environment in the city of Leuven, Belgium. For glass samples with self cleaning (SC) coating, and multilayer (ML) coatings, the transmittance reductions were found to be 1.30%, and 0.85%, respectively, while the uncoated glass sample showed 2.63% transmission loss. Although thorough performance evaluation of these coatings and their durability were not reported, the glass sample with multilayer (ML) coating showed better performance over three weeks of exposure. For photovoltaic modules exposed to outdoors in Arizona, 5% efficiency improvement was observed in modules treated with a hydrophilic anti-soiling coating [8]. Piliougine *et al.* [9] evaluated the effect of anti-reflective and anti-soiling coatings on polycrystalline PV modules exposed outdoors for one year at the University of Málaga, Spain. Examination of the electrical parameters of the coated PV modules before and after the coating procedure showed 1-1.5% increase in the maximum power at the given condition due to anti-reflective feature of the coating that increased the transmittance. Transmission losses during summer months increased to 10% for coated and 12% for uncoated PV modules. During the one-year exposure period, coated

PV modules showed average daily soiling losses of 2.5%, while uncoated modules an a daily average of 3.3%. Recently, Hunter [10] reported the application of superhydrophobic coating of CSP mirrors for self-cleaning applications. Anti-soiling coating mainly suffers from three issues: (1) water is still needed for cleaning, (2) their lifetime is limited and is greatly site-specific, (3) re-application of coating might reduce the optical performance, and (4) dust adhesion due to electrostatic coating is not reduced.

Kochan [11] reported robotic cleaning method for windows and Anderson *et al.* [12] developed PVCleaner Robot for cleaning PV modules. PV Cleaning robot consists of two moving trolleys attached to the top and bottom of the modules and one cleaning head moving upward and downward while brushing the surface. During the initial tests, a cleaning rate of 2.33 m^2/min using water at 0.58 l/m^2 was recorded. Since a water-restoring mechanism was employed in surface brushing, efficiency in water usage was improved approximately 100 times compared to deluge water spray cleaning method.

There are some disadvantages associated with robotic devices: (1) it needs water resources/surfactant for cleaning, (2) it is still in developmental stages and scalability of the method in large solar plants is not yet established, (3) it needs a team of technicians for supervision of robot operation, (3) power consumption of the robotic device is not cost effective in some applications, and (4) it has high operation and maintenance costs. Depending upon the regions where solar power plants are located, Mani and Pillai [13] provided a detailed guideline for cleaning PV modules at regular intervals with water and detergent.

INTRODUCTION

Application of transparent electrodynamic screens (EDS) [14 - 20] is an emerging method for cleaning terrestrial solar collectors. An EDS consists of rows of transparent, parallel electrodes embedded within a transparent dielectric film, as shown in Fig. 1. The transparent screen is integrated or retrofitted on the front cover-glass plates of the solar panels or the concentrating solar mirrors. When the electrodes are activated with three-phased voltages, the dust particles deposited on the surface of the EDS become electrostatically charged and are repelled, then removed, by Coulomb repulsion forces. Dust removal on solar collectors is performed without water or moving parts.

Although EDS is an effective method for dust removal, integrating EDS on the surface of a solar mirror or PV module will cause an initial loss of reflection or transmission efficiency simply due to the presence of the electrodes. This initial optical loss will depend upon the choice of

electrode material, electrode geometry, and the properties of the dielectric film encapsulating the electrodes.

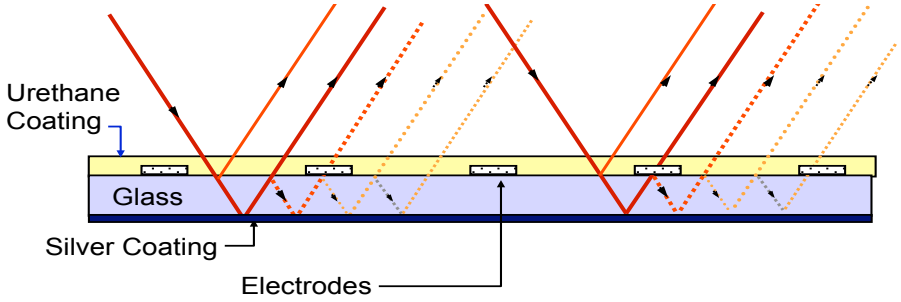

Figure 1. Schematic diagram of an electrodynamic screen integrated on a second surface glass mirror. The electrodes are made of transparent conductive material and are encapsulated in an optically transparent film.

This initial loss should be as low as possible, whereas the dust removal efficiency of the process needs to be highly effective for maintaining a high average optical efficiency of the solar collectors during operation.

We first reviewed the degradation of solar collector performance caused by soiling results and the corresponding loss of energy yield as reoorted by Sayyah et al. [3]. The review includes more than 100 of the major studies reported on energy-yield losses on solar plants in operation in several regions of the world.

Dust accumulation has a more detrimental effect on concentrated solar power systems than on flat-plate PV panels. A portion of sunlight forward scattered by dust particles deposited on a PV surface will be absorbed by solar panels and will produce energy, but a dust layer on a concentrating solar collector, such as a mirror will cause scattering and absorption losses and would not be focused on the absorber. Sayyah *et al.* [21] reported soiling losses in concentrated solar power systems and different cleaning mechanisms used in mitigation of soiling losses.

PROJECT RESULTS AND DISCUSSION

1. Optical efficiency in CSP systems: Concentrating Solar Power (CSP) systems use mirrors to concentrate direct-beam solar radiation onto thermal energy receivers, which can then convert the energy flux into electricity. Parabolic troughs, for example, use receiver tubes enclosed in an evacuated glass envelope. The focused beam from the parabolic trough passes through the evacuated glass envelope to reach a coated steel tube carrying a heat transfer fluid passing through the receiver tube to collect the thermal energy. Similarly, heliostat mirrors are used to

concentrate solar radiation onto power towers to transfer into heat at the receiver and stored thermal energy to be converted into electricity.

Operating CSP plants at peak optical efficiency is one of the key factors for cost-effective plant operation. In a CSP system utilizing parabolic troughs, the desirable specular reflection efficiency (SR) of direct-beam solar radiation is greater than 90%. The reflection efficiency of a clean mirror is typically 93 to 96% prior to installation. Dust deposition and misalignment reduce initial reflectance after installation. The transmission efficiency (TR) of the evacuated glass cover tube likewise needs to be as high as possible. Only a fraction γ of the concentrated beam reaches the receiver tube because of imperfections such as surface texture, misalignment, and tracking errors of the parabolic trough. Finally the absorptivity α of the receiver selective coating determines the energy absorbed by the heat transfer fluid. The product of these four factors yields the peak optical efficiency of the parabolic trough collectors [22] shown by

$$\eta_{opt} = SR \times TR \times \gamma \times \alpha \qquad (1)$$

The optical efficiency η_{opt} of parabolic trough collectors is usually in the range 74 – 79% [22]. The peak optical efficiency, defined at zero-degree incidence angle, plays a major role in the overall performance of the CSP system.

Keeping the solar collectors and receivers in CSP systems clean will maintain η_{opt} at its highest possible level, but cleaning is a major cost component of plant operation. If the availability of fresh water is limited, operation of a CSP plant will become a major competitor for local water resources. Solar plants located in desert areas that happen to be close to the ocean must often resort to the desalination of seawater. The cost of desalination or, alternatively, transportation of large volumes of water to the plant site for mirror cleaning is a limiting factor in the utilization of CSP systems.

Deposition of dust on the front surface of the mirrors causes loss of reflectivity due to scattering and absorption of solar radiation. Because the light must make two passes through a deposited dust layer in transmission and reflection, as shown in Fig. 2, both scattering and absorption will occur twice in the optical path. The scattering and absorption of solar radiation by dust particles are functions of both wavelength and dust properties such as size, shape, and chemical composition. Degradation of specular reflectivity and transmission efficiency results in loss of energy-yields and revenue. Losses of transmission efficiency, reflectivity, and energy yield have been reported by many authors for solar plants in different parts of the world [2, 23, 24].

1.2 Atmospheric dust deposition: Aerosol particles in the atmosphere include (1) dust stirred up and blown from the ground by wind, (2) road dust generated by friction between rubber and

the road, and other mechanically produced dust particles such as agricultural activities, (3) salt particles from seawater spray that occur as the droplets evaporate, (4) anthropogenic particles such as particulate pollutants discharged from power plants, (5) biological particles such as spores and pollens, (5) photo-chemically produced particles of sulfates and nitrates, and (6) soot particles from forest fires, automobiles, and volcanic eruptions.

In general, atmospheric particles have a tri-modal size distribution. As most of the particles are produced at or near ground level, their concentration decreases almost exponentially as a function of height, and most of the particles suspended in the atmosphere are within a height of about 1.5 km from the ground level. The particle size range can be divided into three categories:

(*i*) Ultrafine: $d_p < 0.1$ μm,
(*ii*) Intermediate: $0.1 < d_p < 3.0$ μm,
(*iii*) Coarse: $d_p > 3.0$ μm

(*i*) Ultrafine dust particles ($d_p < 0.1$ μm) remain mostly in the atmosphere and have a low deposition rate that is limited by the diffusion process. Their deposition on the collector's surface depends upon the diffusion process. For subwavelength particles in this range, the extinction coefficient can be neglected compared to that of intermediate and coarse particles.

(*ii*) Intermediate-range particles ($0.1 < d_p < 3.0$ μm) are always present in the atmosphere, and their deposition on the solar collectors cause significant optical loss. Since this size scale is comparable to the solar-radiation wavelength, intermediate-range particles can be efficient in scattering and absorption, depending upon their complex refractive indices. The extinction coefficient Q_{ext} is a function of particle parameter x_p ($\pi d_p/\lambda$); as x_p increases, Q_{ext} reaches a value of 2. For a spherical particle of diameter 3 μm, and wavelength 0.5 μm, where x_p is approximately 18 and Q_{ext} is 2. As the particle diameter becomes smaller (< 0.5 μm) x_p is smaller than 2 in the visible and IR regions, Q_{ext} decreases rapidly. For $d_p < 0.1$ μm, the extinction coefficient has such a low value that the presence of such particles does not significantly change the reflection efficiency.

(*iii*) Coarse particles ($d_p > 3.0$ μm): For these large particles, x_p ($\pi d_p/\lambda$) > 10, and scattering in the forward direction becomes much stronger than in any other direction. Most of the scattered energy becomes confined to the forward lobe within an angle of about 0 to 1° degree. Except for the shading loss, the forward scattered beam is nearly parallel to the incident beam.

1.3 Size distribution of dust particles in arid and semi-arid areas: Little information is available with respect to the size distribution or composition of dust particles deposited on solar collector surfaces. Al-Hasan [25] measured size distribution of sand dust particles under normal environmental conditions and reported a mass median diameter of 6.44 μm with a standard deviation of 4.0 μm. Dust storm conditions were not studied. Similar studies show median diameters of dust particles in the range 3 to 6 μm. A detailed analysis of Aeolian atmospheric dust particles that includes dust particle concentration, wind velocities, dust deposition and accumulation rates, and particle size distribution was carried out by Goossens [3] and Offer in the Israel Negev Desert. They reported that most of the particles were in the diameter range 1 to 5 μm and were deposited by impaction with coarser particles deposited by sedimentation. More data on both size distribution and the dust-mass concentration deposited as a function of time are needed to estimate the anticipated specular reflection loss in various solar fields, so as to predict the cleaning frequency required for maintaining high optical efficiency [26].

1.4 Dust deposition rates in deserts and in semi-arid areas*:* Information on the dust deposition rates in current and prospective locations of solar plants is also scarce. Lack of information on dust deposition rates and particle size distribution makes it difficult to calculate the cost of cleaning solar collectors for maintaining desired optical efficiencies. Dust deposition rate vary widely and depend on location, time of the year, and year-to-year variation. Deserts in the Middle East and North African (MENA) regions have an average dust deposition rate of approximately 0.36 g/m^2/day. In the Negev Desert area, for example, the measured dust deposition rate is about 60 to 120 g/m^2/yr; in the Mojave Desert, the deposition rate [4] is somewhat less at about 30 g/m^2/yr. In the southwestern regions of the US, the dust deposition rate [5] is approximately 4.3 to 15.7 g/m^2/yr based on data over a five-year average; the highest rate of dust deposition in Southern California often reaches 30 g/m^2/yr. Composition of deposited dust includes soluble salts, carbonates (gypsum dust) and marine sulfates mixed with coarse sand and silt particles that are locally derived. In the Mojave Desert area, the basic composition of dust particles consists of fine (silt and clay) particles with $d_p < 20$ μm, comprising approximately 33% of the Aeolian dust. The remaining 67% comprise coarse sand particles.

1.5 Power Law distribution and residence time of the particles in the atmosphere: In a limited size range that includes particle sizes of interest for meteorological applications, a power law distribution can be used for particle size:

$$n_d(d_p) = A d_p^{\,m} \qquad (2)$$

where A is a constant, and m is an exponent factor that is usually negative. For suspended particles in the atmosphere, $m = -4$. Such a size spectrum is called a Junge distribution. The residence time for these particles in the atmosphere, $\tau_p \approx d^{-2}$, which means that the residence time

of the coarse particles will range from minutes to hours depending upon atmospheric turbulence. Finer particles will have longer residence times. High wind velocity, dust storms, and dust devils can carry large particles up to 100 μm in diameter.

Size distribution of deposited particles: The fractional mass of fine particles that deposit on solar collectors is small compared to that of coarse particles, since deposition velocity is proportional d^2. However, the extinction coefficient Q_{ext} for particles in the diameter range 0.2 to 3.0 μm is high, because d in this size scale is comparable to the wavelength of the solar radiation. Also, the specific surface area (surface area per unit mass) is higher for the smaller particles. The deposition rate due to gravitational settling increases as d^2, and the rate of deposition due to diffusion increases inversely with particle diameter d. Dust collection on the surface is a dynamic equilibrium conditions between the rate of deposition by gravitational, impaction, and diffusion forces and the rate of removal by wind. Adhesion of dust on the surface is a major factor in the removal process by wind.

2. Adhesion of dust on the surface of solar collectors: Once a dust particle deposits on a surface, such as the surface of a mirror, it experiences several forces of attraction with the surface in contact. The forces of attraction include:

(1) van der Waals force $F_{vdw} = A d_p/(12\, z^2)$,
(2) Electrostatic attraction force: (a) the image force (F_{im}) of attraction if the particle is electrostatically charged $F_{im} = q^2/(16\, \pi\, \varepsilon_o\, \varepsilon_d\, \delta^2)$,
(3) Lewis acid/base force (F_{AB}) that depends on the electrostatic charge exchange between the particle and the surface (electron donor – acceptor interactions which include hydrogen bonding),
(4) Capillary bridge force caused by adsorbed moisture layer $F_{CB} = 2\pi d_p \gamma \cos\theta$,
(5) Gravitational force, $F_g = m$ g, and
(6) Chemical bonding force which is generally present when there is a combination of high RH and deposited dust particles containing soluble inorganic and organic salts, subjected to a long residence time of contact.

The total adhesion force can be written as:

$$F_{adh} = F_{vdw} + F_{im} + F_{AB} + F_{CB} + F_g \qquad (3)$$

where d is the particle diameter, q is the electrostatic charge on the particle, z is the separation distance between the particle and the surface, γ is the surface tension of the liquid (water in this case) on the surface, θ is the contact angle, and A is the Hamaker Constant which depends upon the materials involved and is approximately 5×10^{-20} J for many common materials.

The factors $\varepsilon_{d,}$ and ε_o represent the dielectric constants of the film encapsulating the electrodes (Fig. 1) and that of free space, respectively. The image force F_{im} depends on the thickness δ of the dielectric film *h*aving dielectric constant ε_d. The plane of the conducting electrodes is considered to be a ground plane for the purpose of calculating the image forces. The separation distance between a particle having charge q and its image charge $-q$ is approximated by 2δ in the equation for the image force F_{im}.

The forces of attraction between a dust layer and a flat EDS panel include both gravitational (F_g) and sum of adhesion forces. The primary forces of attraction are the van der Waals, capillary, and electrostatic forces. At a low RH < 60%, the capillary force of attraction is relatively small. If the surface of the EDS has a superhydrophobic coating, the capillary force can be neglected even at RH > 90%.

At the initial contact between a dust particle and the EDS film surface, the separation distance z is generally limited to only a few asperities on the surfaces. The van der Waals force thus decreases rapidly as the distance of separation increases, and it nearly vanishes when $z > 100$ nm [27]. For most cases, the separation distance is assumed to be 0.4 nm. After contact is established, the van der Waals and the electrostatic forces can deform the particle shape and reduce asperities, particularly in the case of soft materials, and reduce the separation distance while increasing the area of contact. This deformation and the associated increase of adhesion force is a function of the residence time of contact.

3. Loss of Optical Efficiency Caused by Dust Deposits on Solar Mirrors:

It is possible to estimate overall reflection losses caused by the deposition of dust particles on the mirror if the particle size distribution (PSD), the extinction coefficient for the particles, and surface mass concentration in g/m^2 are known. The extinction coefficient Q_{ext} of a particle is the sum of its scattering efficiency (Q_{sca}) and its absorption coefficient (Q_{abs}) [27, 28]. The extinction coefficient varies from 0 to 5, depending on the particle size parameter x_p ($x_p = \pi d_p/\lambda$), the particle shape, and the complex reflective index m ($m = n - ik'$), with n being the real component of the index of refraction, and k' being the imaginary part for the wavelength λ of the incident radiation. The values of n and k' are called the "optical constants" of the material, although these are functions of the wavelength of radiation. Since the absorption $Q_{abs} = 4\pi k'/\lambda$; there is no absorption loss when $k' = 0$.

Based on the diameter d_p of the particles and the refractive index m for a given wavelength λ, it is possible to determine the values of Q_{sca}, Q_{abs} and Q_{ext} from Mie scattering theory. The extinction coefficient Q_{ext} is the ratio of the energy removed due to scattering and absorption by the particle, to the energy incident geometrically on the particle. Thus, the extinction efficiency of the particle

times its projected area A_p is the cross sectional area of energy removed from the beam by the particle through scattering and absorption.

For a cloud of dust particles or a dust layer of deposited particles, it is possible to write an expression for the attenuation coefficient as

$$\alpha = \Sigma Q_{ext} = \Sigma Q_{sca} + \Sigma Q_{abs,} \quad (5)$$

by summing the losses caused by individual particles. The loss of light transmission through the dust cloud can be written following Beer's law:

$$I = I_o \exp(-\alpha L) = I_o \exp \Sigma_i N_i \pi d_{pi}^2 (Q_{exti})/4 \quad (6)$$

Here L is the optical path length of the light as it travels through the dust cloud, and N_i is the number concentration of particles having diameter d_{pi} residing in the optical path. For monodisperse spherical particles of diameter d_p, the attenuation coefficient of the dust cloud can be written as:

$$\alpha = \mathrm{N}\, A_p\, Q_{ext} = N \pi d_p^2 (Q_{ext})/4 \quad (7)$$

where N is the number of particle per unit area in the optical path of incident beam. The same expression (eq. 7) is valid for a dust layer of monodispersed particles deposited on a transparent substrate. The number density of the particles is assumed to be low in the dust layer so that there is no significant multiple scattering. For monodisperse, spherical dust particles of diameter d_p, the volumetric mass concentration C_m (kg/m^3) and the number concentration N per m^3 are related by

$$C_m = N \rho_p \pi d_p^3/6 \quad (8)$$

where ρ_p is the particle mass density in kg/m^3. Generally, the surface-mass density of a dust layer on a substrate is expressed as g/m^2; the number of particles per unit area can be calculated from $C_{m,}$ assuming all the particles are of the same size and mass density.

3.1 Transmission Loss: For a monolayer of uniform dust particles of diameter d_p, deposited on the surface of a solar panel, the attenuation of light can be calculated using the following equation, where N is the number of deposited particles per unit area*:* $\alpha = \mathrm{N}\, A_p\, Q_{ext}$, and the attenuation of light intensity for the case of monodisperse particles can be written as

$$(I/I_o) = e^{(-NA_p Q_{ext})} \quad (9)$$

For polydisperse particles, the product $NA_p Q_{ext}$ can be written as

$$NA_pQ_{ext} = \Sigma_i \pi(N)_i (d_i/2)^2(Q_{ext})_I \qquad (10)$$

where $(N)_i$ is the particle number concentration, with diameter d_i having extinction efficiency $(Q_{ext})_i$.

3.2 Reflection Loss: The reflection loss for second-surface glass mirrors can be calculated from equation (9). As shown in Fig. 2, the light rays pass through the dust layer twice, once as the incident beam enters through the dust layer, and a second time as the reflected beam passes through the dust layer on to the receiver:

$$(I/I_o) = e^{(-2NA_pQ_{ext})} \qquad (11)$$

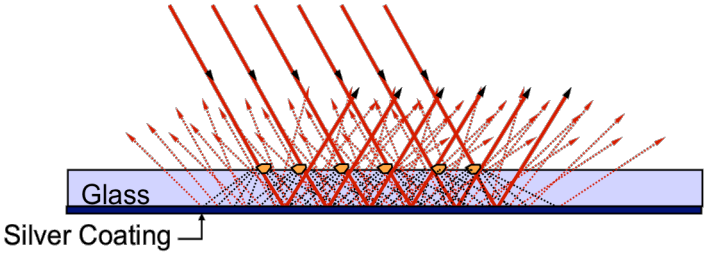

Figure 2. Reflection loss caused by two passes through dust deposited on second surface mirrors.

For the purpose of analyzing Q_{ext} as a function of d_p and λ, it is possible to calculate extinction as a function of the particle size parameter x_p $(\pi d_p/\lambda)$ following Mie scattering theory [28], assuming the particles are spherical in shape.

3.3 Estimation of Specular Reflection Loss: For particles of size $d_p > 3.0$ μm, the extinction coefficient $Q_{ext} = 2$, which means that each particle removes light over twice the area it intercepts $(2A_p)$. In practice, however, when the distance between the CSP mirror and the receiver is short, as is the case with a parabolic trough, the diffracted light suffers only a small deviation from the original rectilinear propagation, with angular deviation often much less than 2^o degrees. Depending upon the acceptance angle of the parabolic trough [23, 24], the diffracted light will be within the theoretical minimum acceptance angle of 25 mrad ≈ 1.4^o degrees. At least a significant portion of the forward scattered light from large particles will reach the receiver tube. For a parabolic dish, it is possible that the deviation of the diffracted light from large particles will be within the acceptance angle of concentrating parabolic mirrors. For heliostats, however, the required acceptance angle is only 3 mrad. Consequently, there will be a larger reflection loss caused by dust deposition [29 – 30].

It is possible to estimate overall reflection losses caused by the deposition of dust particles on the mirror if the particle size distribution (PSD), the optical constants (*n* and *k*'] for the particles, and surface mass concentration in g/m^2 are known. Experimental studies show that for particles having < 0.5% of carbon content and other absorbing components, it is possible to assign the value $k' = 0.001$, as shown in Table 1 [28 - 30].

Table 1. Major mass fraction of atmospheric particulate matters likely to be deposited on solar collectors in desert and semi-arid areas

Constituents	Size range (Diameter)	Dust composition percent in arid and semi-arid areas	Estimated values of k' in the visible region
Quartz, Calcite, oxides of iron, Clay minerals,	1 – 10 μm (larger particles >10 μm under high wind and dust storms	30% or more depending upon location and weather conditions	*k'* values of the mixture of particles is 0.001(approx..)
Salt and organic particles	1 – 10 μm	10 – 15%	$k' < 10^{-5}$
Absorbing particles	< 3 μm except for Fe_2O_3	Soot Particles, Fe_2O_3	$k' \approx 1.0$ $k' > 1.0$ for Fe_2O_3

4. Modeling of Loss of Optical Efficiency Caused by Dust Deposition on Solar Collectors:

A comparative study was made between (a) loss of reflectivity caused by EDS integration on the mirror and (b) dust layers on the optical surface causing reflection losses by light scattering and absorption. An optical engineering software program named "FRED" was used to perform comparative studies between optical losses caused by EDS integration, and by deposited dust. The FRED software is a product made by Photon Engineering.

In Figs. 3 and 4, we show the reflection loss vs. surface mass concentration of accumulated particles of 5 different diameters: 3, 5, 10, 20, and 30 μm. The graph was plotted using the FRED

optical software. Particles were assumed to be spherical. We have also plotted the combined effect of surface mass concentration of dust particles containing composite particles (shown as Comp) of these five different sizes following the Junge mass distribution model [27] of atmospheric dust. The figure shows that as the particle size decreases, for the same surface-mass concentration, the total surface area of the particle increases, thereby causing more loss in specular reflection. The reflection loss caused by the composition of particles is more realistic for practical applications. Taking the reported data on maximum dust deposition rates in the Southwest US regions, it appears that solar mirrors may suffer as high as 50% loss over a period of one month.

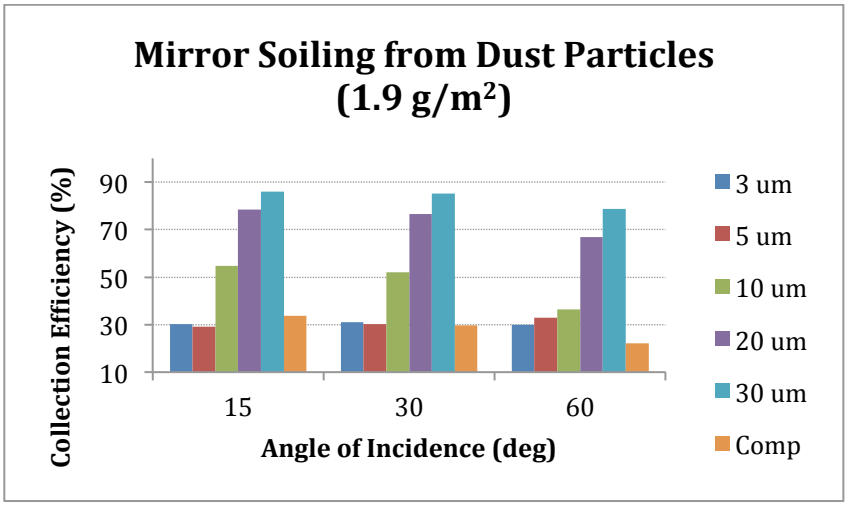

Figure 3 - Reflection losses for a known surface mass concentration (1.9 g/m^2) of deposited dust on the mirror surface comprising dust particles of different diameters. As particle size decrease, the specific surface area per unit mass increases, causing higher loss of specular reflectivity.

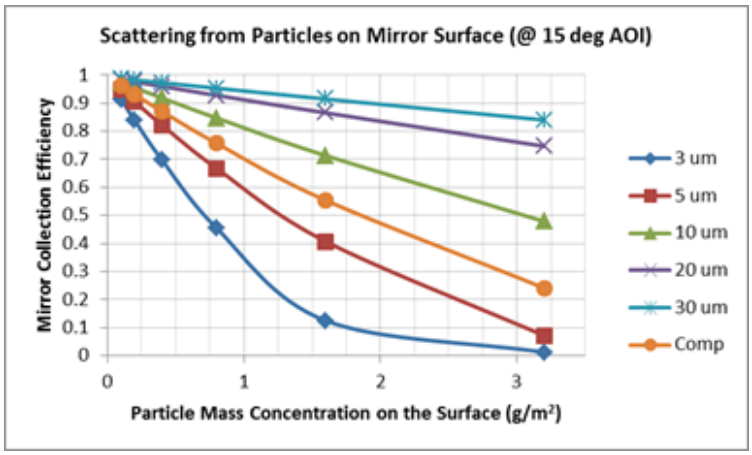

Figure 4 - Reflection losses caused by scattering of particles of five different diameters as a function of surface mass density of deposited particle. The loss marked as "Comp" represents a composite of particles of the five different diameters in mass proportion that follow a Junge distribution of atmospheric particles.

The model prediction is in agreement with Equation (11) showing that reflection loss decreases exponentially as the sum of the products of projected area and extinction coefficient (NA_pQ_{ext}) increases.

The relationship between specular reflection loss and the surface mass distribution of deposited dust were determined experimentally using Mars dust simulant JSC-1 (Fig. 5). This test dust contains mostly SiO_2 Al_2O_3, TiO_2, FeO, Fe_2O_3, CaO, Na_2O_3 with a wide particle-size distribution. JSC-1 dust is available commercially and is often used as a "standard" dust. For our application, the dust was sieved for particle diameter < 40 μm with a mean diameter of 15 μm. Specular reflection efficiency was measured using a non-contact reflectometer.

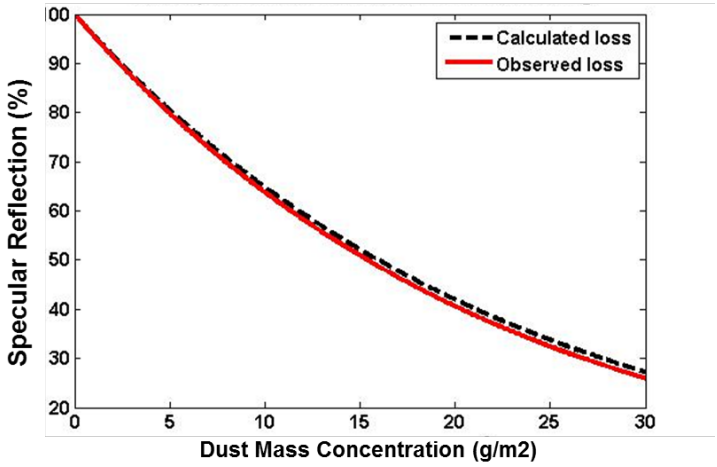

Figure 5 - Specular reflectance vs. dust-mass concentration for a second surface silvered mirror.

Our studies show that most of the particles deposited on solar collectors operating in semi-arid and arid regions will be in the diameter size range 2 to 50 μm. Finer particles will have larger specific surface areas (surface area per unit mass) and will cause higher reflection loss compared to dust particles of larger diameter.

5. Energy Required for the Removal of a Deposited Dust Layer:

Because operation of electrodynamic screens (EDS) involves electrostatic charging and removal, operation of the EDS may be limited to RH less than 50%. When the RH greater than 50%, the primary forces of attraction will be the van der Waals and the electrostatic image forces. For highly charged particles larger than a few μm in diameter ($d_p > 2$ μm), the electrostatic attraction force dominates over the van der Waals force. For removing dust deposited on the surface of the EDS surface, the dust particles are charged to a high level and then repelled and transported away by the electrostatic Coulomb forces at the surface. For a deposited dust layer not exposed to high humidity, the electrostatic adhesion force F_{im} exceeds all other forces of adhesion for $d_p > 2$ μm.

The energy required for removing a dust layer from a solar mirror can be calculated based on dust deposition rates. For example, in the southwestern United States, the estimated surface-mass concentration of dust is estimated as 1.9 g/m^2 over 3 weeks. Assuming a density of sand particles of 2300 kg/m^3 and a mean particle diameter of 3 μm, the energy required for lifting the dust layer by 1 cm and then removing it would be approximately 2.3 x 10^{-3} J per square meter of mirror over 3 weeks. This is an imperceptibly small amount of energy if the removal forces can be applied directly to the particles, as is the case for an electrodynamic screen.

6. Prototype Developments and Evaluation of Transparent Electrodynamic Screens:

In this section we present a brief discussion on producing a prototype EDS for direct integration on the surface of the mirror or for retrofitting the EDS onto the mirror surface. An electrodynamic screen consists of rows of parallel electrodes embedded within a transparent dielectric film and laminated on the front surface of solar panels or mirrors. A schematic diagram of an EDS is shown in Fig. 6. When phased voltage pulses activate the electrodes, the dust particles on the surface become electrostatically charged and are removed by the traveling-wave generated by the three-phase alternating electric field. Over 90% of deposited dust can be removed within two minutes, using a very small fraction of the energy produced by the solar collector. The power output is restored to 95% or better compared to the power obtained under clean conditions. No water or mechanical wiping is involved.

6.1. EDS configuration: The transparent electrodynamic screen (EDS), consisting of a series of transparent inter-digitated electrodes embedded in a transparent dielectric film, can be used as a viable dust mitigation system for removing dust particles from solar-collector surfaces. Since Coulomb force is the predominant force in repelling the deposited dust repels particles once they acquire electric charge, having electric field distribution model of the EDS is of utmost importance [31, 32]. For the modeling of the electric field distribution of the EDS, we have considered several EDS configurations. The following figure shows three of the configurations studied.

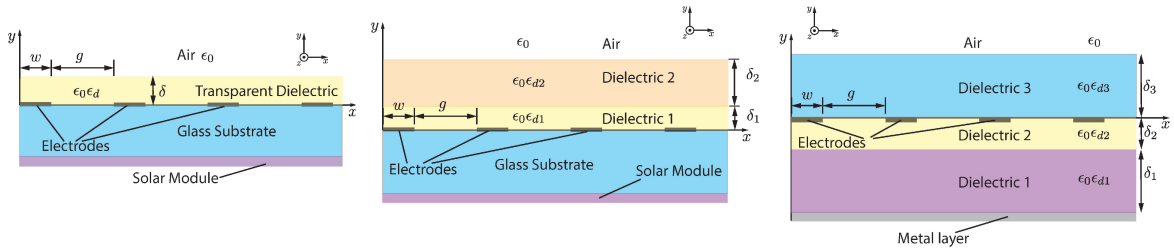

Figure 6. Three configurations for the EDS considered in the course of studies.

The closed-form analytical solutions for the electric field distributions for the EDS configurations with one and two layer(s) of dielectric coatings have been provided It has been clearly shown that the electric field distribution on the EDS surface, where the dust particles accumulate, are dependent upon the electrode width, inter-electrode spacing, thickness of the dielectric layer(s), relative permittivities of the transparent layer(s) as well as operating voltage. The closed-form analytical solutions provided for the electric potential and electric field distribution have been corroborated using COMSOL® Multiphysics® Finite Element Analysis (FEA) software.

Deposited dust particles are exposed to the non-uniform electric field, generated by the deposited electrodes. This non-uniform electric field leads to dielectrophoresis phenomena by the divergence of the electric field. The field is both spatially nonuniform and time variant. The dielectrophorectic (DEP) forces exerted on the particles are not dependent upon the particle charge. Thus the DEP forces on an uncharged particle could cause translational and rotational motion on the surface of EDS and cause triboelectric charging of the deposited particles. A closed-form solution for the electric field distribution are derived [33].

As mentioned previously, the electric field distribution on the EDS surface is dependent upon the geometric parameters, including electrode width and inter-electrode spacing. One of the goals of the developing EDS technology is to improve its performance in removing dust particles. Different objective functions for the electric field distribution on the EDS surface were

considered and the optimal values for the electrode width and inter-electrode spacing were determined.

As noted previously, Coulomb force is the dominant mechanism in dust particle removal from EDS surface. The charge of the dust particles is another key element in performance evaluation of the EDS. Comprehensive experimental studies were conducted in an environmentally controlled test chamber to examine the charge to mass ratio of the removed dust particles as a function of the electrode width, inter-electrode spacing, and operational parameters such as relative humidity and the applied voltage. For this test, twelve EDS samples with different electrode width and inter-electrode spacing were developed.

7. Construction of prototype EDS mirrors by an integration process: Prototype transparent electrodynamic screens (EDS) were constructed by depositing rows of transparent parallel electrodes made of transparent conducting materials, 70 μm in width, 750 μm inter-electrode spacing, and an electrode thickness of 1 μm. The electrodes were deposited directly on the front surface of the solar collectors and were embedded within a transparent dielectric film having a thickness of 50 μm [Fig. 7]. In some of the experimental studies, a conducting polymer PEDOT:PSS [poly(3,4-ethylene-dioxythiophene) poly-(styrenesulfonate)] was used and the electrodes were deposited by using screen-printing techniques [15, 16]. In this phase of the study, two dielectric materials were used for encapsulation: urethane film applied using a Meyer rod coating process, and a UV-stabilized acrylic film laminated on the surface of the solar collectors using optically transparent adhesive film.

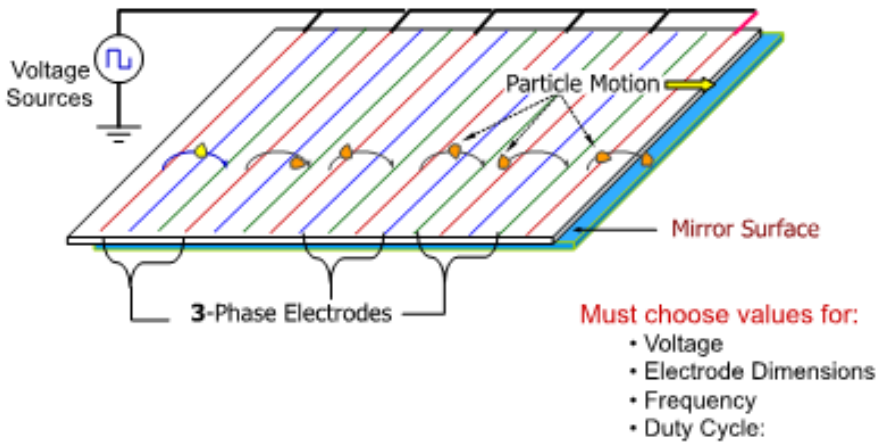

Figure 7. Schematic representation of an electrodynamic screen showing a pattern of parallel electrodes for 3-phase pulsed voltage drive.

7.1 EDS-integration during the manufacturing process: For direct integration of EDS on a flat surface, the electrodes can be printed using a screen-printer or a gravure offset printer for patterning the lines on the glass surface of the solar collector, which is either a second surface mirror or the glass cover plate of a PV module [17, 18]. The electrodes vary from 50 to 100 µm in width with an inter-electrode separation of 500 to 800 µm. A three-phase, pulsed high-voltage supply is used to activate the electrodes. The amplitude of the pulsed high voltage is usually in the range of 700 to 1200 V at a frequency of 5 to 100 Hz.

7.2 EDS film production for retrofitting: In order to construct an EDS suitable for all surfaces regardless of curvature, a fabrication process has been developed that first prints the EDS electrodes on a highly transparent, flexible substrate as a film. The latter is then applied to the curved or flat surface using an optically clear adhesive. Figure 8 shows an EDS film stack composed of electrodes made of transparent conducting materials, an optically clear adhesive film, and a transparent dielectric film that encapsulates the electrodes on the surface of the mirrors. Figure 9 shows a photograph of a prototype EDS film.

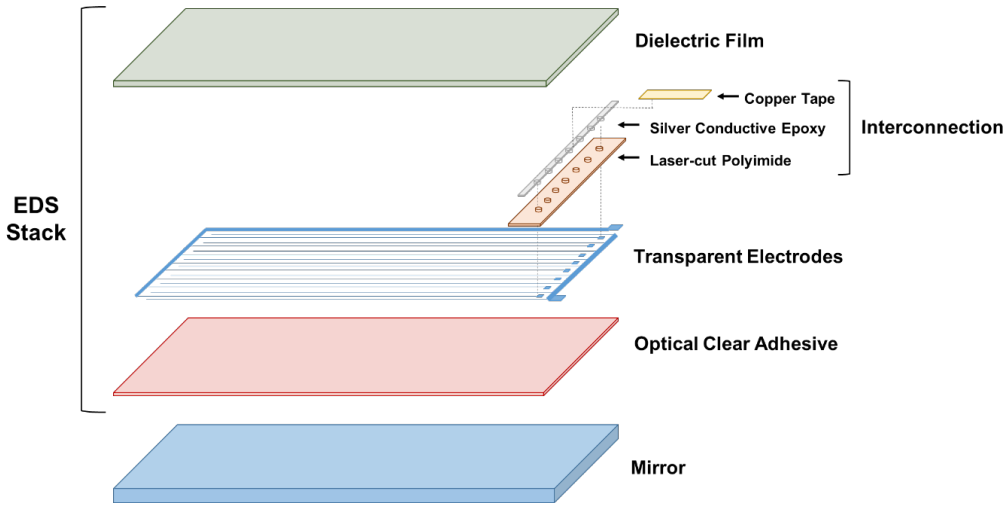

Figure 8 - Construction of EDS stack for integration or retrofitting on a second surface mirror.

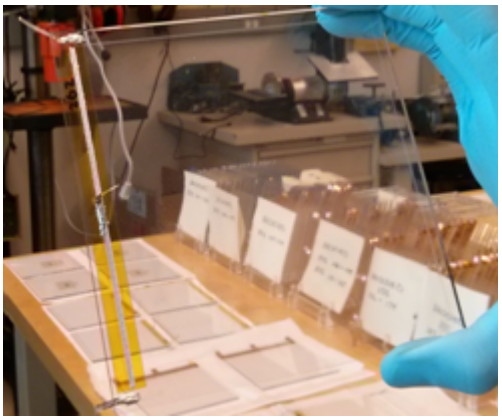

Figure 9. Photograph of the EDS film with silver nanowire electrodes

8. Electrostatic Charging Process in EDS:

Different mechanisms involved in the electrostatic charging process were reviewed [34-35]. Our review shows that several processes may simultaneously contribute to the electrostatic charging of the particles. These include (1) contact charging based on the surface states of particles in contact with the dielectric film surface, (2) turboelectric charging process caused by Coulomb- and dielectrophoretic (DEP) force induced motion and rolling particles, (3) electrostatic breakdown discharge (DBD) and (4) corona charging. In all cases, surface charge leakage is necessary to regenerate the neutral state of the dielectric film surface aided by charge injection from the surface.

However, the processes responsible for charging particles, either individually or collectively, should produce a bipolar charge distribution of both positively and negatively charged particles. In experimental studies, we found that the particles are mostly charged with positive polarity. In the absence of EDS activation, triboelectric charging between the test dusts and EDS film produced a net negative charge-to-mass ratio [35]. With electrodes embedded within a dielectric medium and activated with high voltage pulses, no visible dielectric breakdown discharge was observed in a darkroom. The experiment was conducted to observe the presence of surface barrier discharge or corona discharge generating positive air ions and electrons.

Based on our research, we present the hypothesis of a filamentary microdischarge process responsible for charging the particles on the surface of the EDS film, primarily with positive polarity. As the electric field increases to the incipient surface ionization point at the edges of the electrodes, microdischarge filaments are formed (Fig. 10) due to the formation of a weakly ionizing field [36]. It is believed that a large number of individual, tiny microchannels are formed. Within sub-microsecond duration, the field is reduced significantly due to the space

charge created by the field surrounding the electrode edge. The breakdown discharge is interrupted momentarily. The spatial distribution of the microchannels changes to allow the next ionization event, and the process is repeated until the applied voltage reaches its maximum level. When the electric field strength decreases below the ionization level, the plasma discharge process is no longer sustained. As the localized electric field at the edge of the positive electrodes exceeds the ionization point within the dielectric medium, microfilaments are produced momentarily, at the interface between the glass surface and the dielectric film encapsulating the electrodes. The charge carriers contain both electrons and positive ions around the edges of the electrodes. Electrons migrate rapidly to the positive electrode with a much higher drift velocity compared to that of positive ions and holes moving in the opposite direction. Each time the microdischarge quenches (< 0.1 μs) it leaves positive space charge. During this time interval, the positive charge and the energy created by the microdischarge are distributed over the entire surface of the dielectric layer [36].

The electrodes are deposited on a glass surface, as shown in Fig. 7, (such as a second surface mirror or a cover glass plate of a PV module). The micro-discharge occurs at the edges of the positive electrodes in response to the applied low frequency high voltage pulses, as explained above. The positive charges migrate towards the surface of the EDS under the influence of the traveling electric field. As the voltage drops with each cycle, the discharge stops. In the next cycle, the same channels are created due to the "memory effect" [36]. The process continues to repeat at the low frequency of the high-voltage pulses.

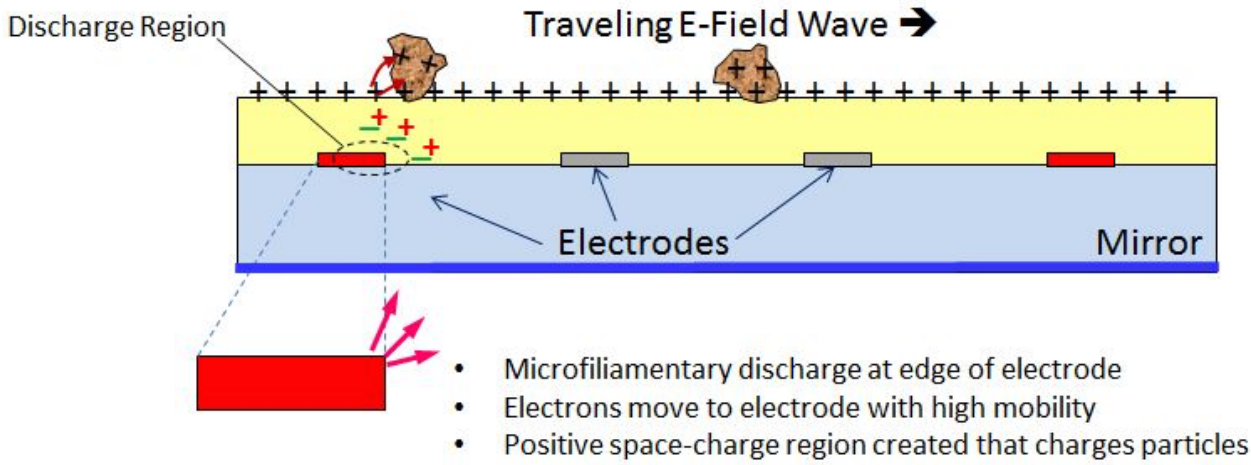

Figure 10 - Depection of a filamentary microdischarge process at the interface of glass and a dielectric medium surrounding the electrodes.

At the negative electrodes, a similar charge migration phenomenon does not occur, because the migration velocity of positive ions is low compared to that of electrons. At the end of each cycle,

at the negative electrode edge, positive and negative electrons are created, and they recombine rapidly because of the higher mobility of electrons; there is no net negative space charge left surrounding the electrode. The positive ions have a low migration velocity and do not reach the surface of the negative electrode immediately as the breakdown discharge occurs. At the end of the discharge cycle, the electrons near the electrode surface neutralize the positive charges. At the negative electrodes, the positive ions and negative electrons are generated but are rapidly neutralized at the end of the cycle.

There is a high concentration of ions (for example, Na^+ in borosilicate glass, surface moisture trapped on the glass surface, and in the ionic polymer film encapsulating the electrodes) in the dielectric material surrounding the electrodes.

The charge conduction process can be considered as the drift and diffusion of positive ions to the surface (ion current) or the holes migrating from the charge traps to the surface (hole current). In a polymer, there is a high concentration of charge carrier traps caused by materials added in the polymerization process. Thus it appears that the conduction process in a polymer can be considered to be similar to that of a doped semiconductor. The energy traps in a polymer (which could be as high as $10^{23}/m^3$) can aid conduction by the drift currents of electrons and holes Another way to visualize the physical process is to assume that the electrons migrate rapidly from the surface to the positive space charges in the discharge region during each cycle leaving positively charged particles.

Atten, et al [37] attributed the charging of particles on the electrodynamic screen to the dielectric breakdown discharge (DBD). They studied bare electrodes on the surface and applied voltages from 0 to 6 kV using a single-phase screen with the applied AC high-voltage. They explained that as the applied voltage reaches the inception electric field of DBDs, there are partial discharges in the air that create gaseous ions (positive and negative) and electrons; for each local partial discharge, the field drives the charge carriers to two regions of area restricted to the top surface of the particle layer. At ambient air pressure, the concentrations of ionic and electronic charge created by each DBD on the surface are high enough to promote efficient charging of the particles with positive and negative polarities.

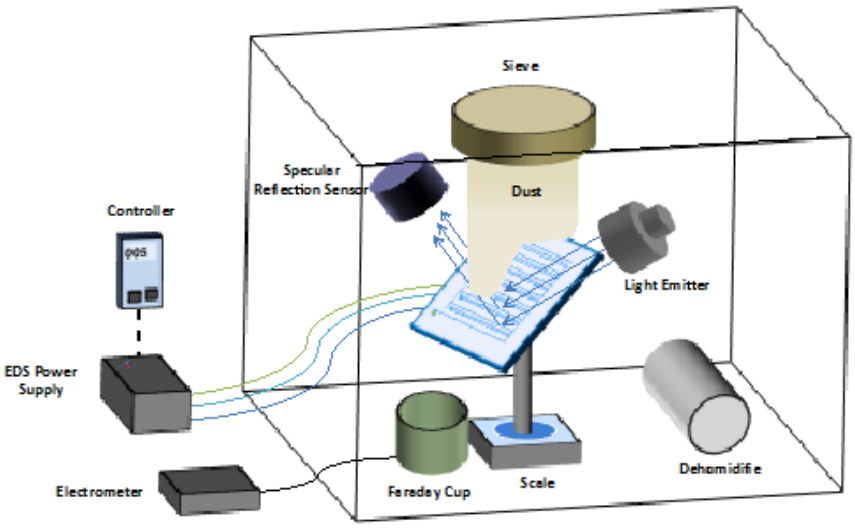

Figure 11. Experimental arrangement for measuring charge-to-mass ratio (Q/M) of removed paticles and specular reflection efficiency of EDS mirror.

8.1 Experimental Data on Charge-to-Mass Ratio: The charge-to-mass ratio of the dust particles was measured using an experimental setup shown in Fig. 11. Figures 12, 13, and 14 show the Q/M ratio of the dust particles measured under different conditions. The measured values of Q/M show the effects of the electrode geometry and the dielectric material used for encapsulating the electrodes. These results are in a good agreement with the microchannel-aided positive charging hypothesis.

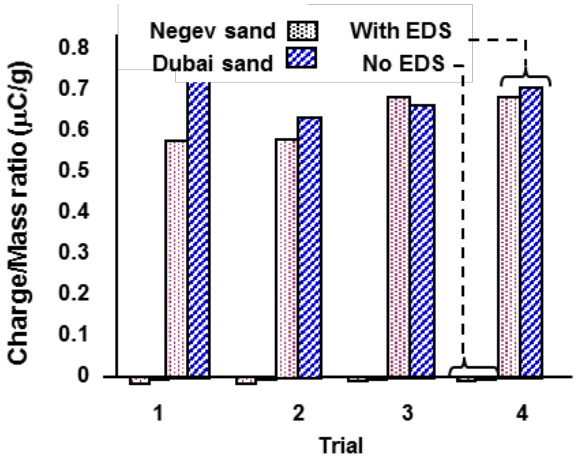

Figure 11 - Measured values of (Q/M) for two different dust samples with and without EDS activation.

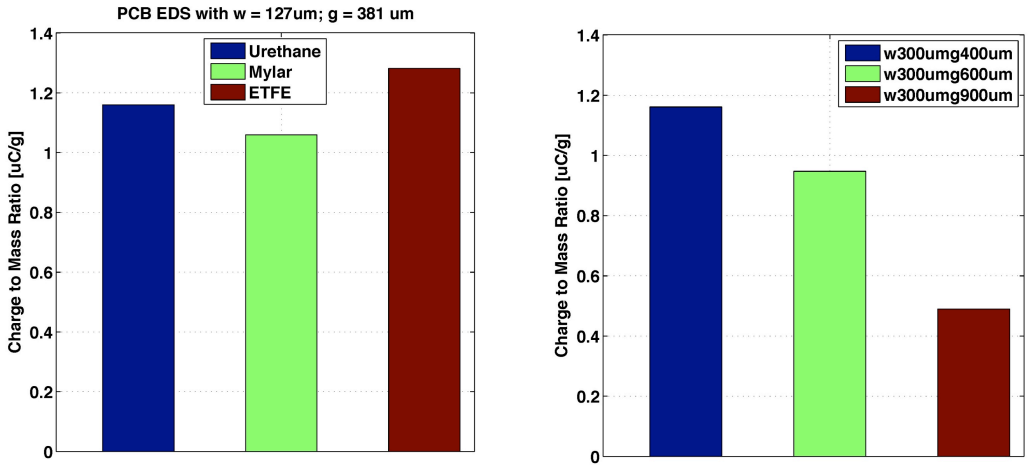

Fig. 12 – (left) Effects of different dielectric materials on measured values of Q/M ratio

Fig. 13 - (right) Effects of increasing inter-electrode spacing on Q/M ratio

The experimwental data show that EDS charges the particles primarily with positive polarity with high efficiency.

9. EDS Design Parameters and Construction Features:

1. Substrates: Second surface glass mirrors, borosilicate glass plates, silvered polymer films (for their application in parabolic troughs and heliostats.)
2. Electrode materials: (a) silver nanowire ink, (b) PEDOT:PSS*, (c) ITO) (d) AZO and (e) silver paste.
3. Electrode dimensions: width (w) = 30 to 75 μm, spacing (s or g) = 700 to 750 μm, thickness (τ) = 1 μm maximum.
4. Electrode printing methods: Screen-printing, gravure offset printing, photo-lithography, and laser ablation.
5. Dielectric film encapsulation: Ultrathin flexible Corning Willow Glass film (100 μm thickness), UV stabilized FEP film, urethane or acrylic film.
6. Fixation to mirror surface: Optically clear adhesive (OCA) film or optically clear liquid adhesive coating.
7. Interconnection for single-layer printing: Currently used for connecting three-phase electrodes to the power supplies for prototype production of EDS film.

9.1 Optimization of EDS Electrode Geometry and Material:

Modeling of initial specular reflection (SR) efficiency losses caused by electrode deposition: The spacing (*s*) and width (*w*) of the electrodes affect both the specular reflectivity loss (ΔRs) and dust removal efficiency (DRE) of the EDS. A high-density arrangement of parallel electrodes with narrow inter-electrode spacing provides optimal electric field magnitude for charging and dust removal, while a large spacing and thin electrodes yields a higher specular reflectivity (SR).

For experimental verification and modeling studies, eight EDS prototypes made from borosilicate glass plates with chromium electrodes were made, with the electrode width varying from 25 to 400 μm and spacing varying from 100 to 900 μm. Each EDS panel served as a second-surface mirror by placing a film mirror (e.g., 3M-1100 silvered film mirror) on the back surface. Chrome electrodes are opaque but have 18% reflectivity. The electrodes were patterned by photolithography for precision control of both the width (*w*) and spacing (*g* or *s*) of the electrodes. A Figure of Merit (FOM) was defined using the ratio of DRE to ΔRs to evaluate the overall performance for different arrangements of electrodes.

9.2 Figure of Merit: $(FOM) = DRE/\Delta R_s$. Ideally, if DRE = 99% and ΔR_s = 1%, the maximum value of FOM will be 99. Our project goal is to have DRE > 90% and ΔR_s < 3%. Thus, if DRE = 96%, and ΔR_s = 3%, FOM would be 32. The higher the FOM the better is the EDS performance. Taking the ratio provides high sensitivity as we design highly effective EDS. It is desired to maintain high specular reflectivity of the mirrors > 90% by increasing *DRE* while still minimizing ΔR_s.

The loss of specular reflectance (ΔR_s) can be measured by using a D&S reflectometer, which is frequently used as a standard instrument in the CSP industries. However, this instrument requires making physical contact with the mirror surface and the base of the instrument. Frequent measurement based on physical contact could cause scratching of the optical surface.

We designed and constructed a non-contact reflectometer for measuring specular reflectance (R_{se}) for each EDS mirror. The initial value of specular reflectivity R_{si} was measured by using a blank glass plate with the silvered film mirror on the back surface. The loss of reflectivity caused by adding the EDS film, consisting of the electrodes and the encapsulating dielectric film, was determined for each EDS film, as $\Delta R_s = R_{si} - R_{se}$.

Dust removal efficiency was measured using the custom-developed dust deposition analyzer to measuring the surface area of deposited particles before and after EDS activation This instrument was designed to measure the total net surface area obscured by the dust particles deposited on the EDS surface both before and after dust removal. It can be used to determine the total projected area of particles (A_{pi}) before EDS activation and the total projected area of the particles (A_{pf}) after

EDS activation. From these two measurements, the Dust Removal efficiency (DRE) was measured, where DRE is defined as percentage of projected particle surface area decreased by EDS cleaning of the mirror:

$$DRE = (A_{pi} - A_{pf})/(A_{pi})$$

The measurements were averaged over the target surface area, which is a programmable feature of the analyzer. The optical setup used for this instrument determines the lower size limit of the dust particles.

The specular reflection efficiency for different electrode configurations was modeled in order to examine the effect of geometry on optical losses. Each of these configurations is shown in the bar graph for four angles of incidence 20, 40, 60, and 80 degrees. From the model analysis, it appears that electrode configuration number 2, (electrode width 75 μm, electrode spacing 700 μm, and thickness 1 μm) provides optimum performance. The calculation was performed for a radiation wavelength of 600 nm.

Table 2 Electrode patterns used for optical modeling of the initial specular reflection loss without dielectric film encapsulation

Configuration	**1**	**2**	**3**	**4**	**5**	**6**	**7**	**8**
Width *w* (μm)	**150**	**75**	**75**	**150**	**150**	**75**	**75**	**150**
Spacing *s* (μm)	**700**	**700**	**700**	**500**	**700**	**500**	**500**	**500**
Height *τ* (μm)	**5**	**1**	**5**	**1**	**1**	**5**	**1**	**5**

The predictions of the optical model on specular reflection efficiency are shown in Fig. 14 for different electrode geometries. Table 2 lists the geometrical configurations of each of the numbers electrode patterns used for optical modeling of the initial specular reflection loss (without dielectric film encapsulation.) The calculations are based on two optical configurations: (1) solar radiation is incident and reflected in a plane parallel to the *y*-axis, and (2) solar radiation is incident and reflected in a plane parallel to the *x*-axis. The *x*- and *y*-axes are shown relative to the electrode geometry in the upper right hand corner of Fig. 14. The specular reflection efficiency is higher when the plane of incidence is along the *x*-axis, as shown by the green bars. When the incident beam is rotated by 90°, and the optical planes are parallel to the *y*-axis, the efficiency decreases, as shown by the red bars. The difference is small, but the model provides an important information on positioning the EDS film on mirrors.

In calculating the above efficiency values for different electrode geometries, the absorption of light within the electrodes was neglected, because the transparency of the electrodes is higher than 90% and the thickness (or height) of the electrodes is very small ($h \leq 1.0$ μm). Only losses caused by the scattering of light (e.g., rays reflected in directions other than that of specular reflection) by the electrodes are considered.

To examine the validity of the EDS optical model, particularly the effects of the dielectric film and electrodes used for constructing EDS on the specular reflectivity, we measured specular reflectivity of (1) clean mirrors without any film or electrodes, (2) mirrors coated with urethane film of 30-μm thickness, and (3) mirrors with PEDOT:PSS electrodes (200 nm thickness), embedded in a dielectric film of thickness 30 μm. The results of these experiments validate the EDS optical model. The effect of surface texture and properties of the dielectric film for minimizing haze was not optimized. Figure 15 shows the effects of 30-μm thick dielectric film used for encapsulating the electrodes (75 μm width, 700 μm separation and 0.5 μm height) and the plane of the incident beam and reflected beam along the x– and y-axes. Commercially available PEDOT:PSS ink (sigma Aldridge and Agfa) was used to produce EDS-integrated mirrors. The electrodes were then covered with a thin dielectric (urethane) film. PEDOT:PSS has high surface energy, which results in the spreading of the ink over the substrate, producing Gaussian-shaped electrodes rather than rectengular. The PEDOT:PSS ink has relatively high resistivity (800 Ω/□) compared to AgNW ink (8 Ω/□).

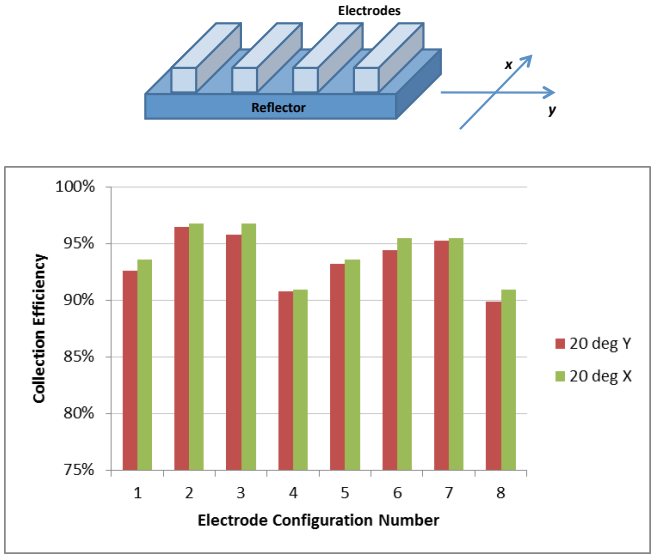

Figure 14 - Calculated values of specular reflection efficiency for two planes; one parallel to y-axis (red) and parallel to x-axis (green) for incidence angle of 20°.

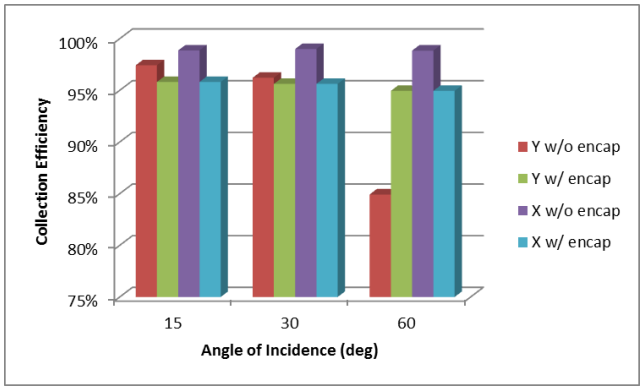

Effects of encapsulation and alignment of EDS electrodes on specular reflectivity as a function of the angle of incidence

38

Figure 15 - Optical model on the specular reflectivity of EDS-mirrors with PDOT:PSS electrodes (500 nm thickness, 75 μm width, 700 μm separation), with and without encapsulating 30 μm–thick PU film.

The performance of the chrome-electrode based EDS with different values of width and spacing was modeled using the FRED optical software. Figure 16 shows a contour plot of the figure of merit FOM ($DRE/\ \Delta R_s$) based on the measured values of *DRE* and ΔR_s. A second-order polynomial was curve fit to the measured specular reflectance values of the mirrors after deposition of the electrodes. The chrome-electrode based EDS parameters are shown as circles on the contour plot to help visualize the optical performance of the EDS geometry for different electrode patterns. The contour plots provide the choice of electrode width and spacing, depending upon the compromise needed for maximizing both DRE and minimizing ΔR_s.

Parameters in the lower right corner of the plot show high optical performance. When the electrodes cover most of the EDS surface, obscuration by the electrodes causes more loss of reflection compared to that of soiling losses. The negative values of FOM have no other physical significance. The white-dotted line represents the thinnest electrodes that can be used if we choose the screen-printing method for manufacturing EDS.

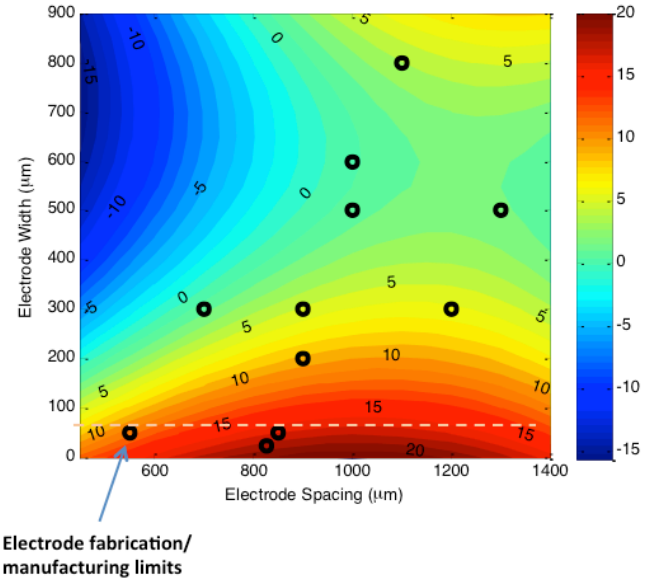

Figure 16. Contour plot of figure of merit FOM (DRE/ ΔRs) based on the measured values of DRE and ΔRs for photolithography patterned chrome electrodes.

From the above optimization studies, it appears that electrode width in the range 25 to 50 μm, with center-to-center spacing of 800 to 900 μm, may provide the best FOM performance for the EDS. Since these optimization studies were performed using chrome-electrode based EDS constructed via photolithography, the measured values of FOM are smaller than what we would expect with transparent electrodes.

9.3 Summary of Electrode Deposition Processes: (1) Screen-printing is the method considered most favorable for prototype development of EDS and for optimizing the process for production of large-scale self-cleaning mirrors, (2) The photolithographic technique is also suitable for large-scale (1 m ×1.3 m) devices. The process is compatible for producing EDS with gallium- or aluminum- doped zinc oxide (GZO or AZO) electrodes, which have the potential to provide both high reflectivity and good dust-removal efficiency. The photolithographic process provides more precise control of the electrode layout compared to screen-printing and ink-jet methods.

9.4 Dielectric film: Urethane is currently used for coating EDS electrodes with film thickness varying from 30 to 50 μm. Other candidate materials include: *(a)* fluorinated/UV stabilized acrylic film, *(b)* ETFE, and *(c)* ultra-thin glass plates.

9.5 Optimization of EDS Electrode Geometry for High Specular Reflectivity and Dust Removal Efficiency:

There are two primary factors that drive the design of electrodes for EDS applications: (1) the electrode pattern, including the materials used to make them so as to remove dust particles efficiently over the size range 0.5 to 50 μm, and (2) desire to minimize the loss in specular reflectivity caused by the presence of the electrodes. In order to obtain high specular reflectivity together with good dust-removal efficiency, a compromise is necessary in the choice of electrode material and the geometrical pattern of the electrodes. The choice of material for the electrodes is also constrained by the method used to pattern them. Screen-printing is a convenient process for low-cost large-scale production but this process is limited to the application of screen-printable electrode materials. Gravure Offset printing (GOP) process requires relatively high initial capital investment, but is more cost effective in high volume production. To help meet this requirement, we limited our choice to one of two transparent conducting inks: PEDOT:PSS (Agfa-Gevaert N.V), and silver nanowire (AgNW) (Cambrios). Other materials that would meet the requirements are indium tin oxide (ITO) and Al-doped Zinc oxide (AZO), but these two materials would require electrode patterning by photolithography.

Table 3 Specular reflectivity and dust removal efficiency of EDS-mirror with PEDOT:PSS electrodes
Specular Reflectivity without EDS integration: 94.2%
Average Specular Reflectivity (%)

Panel	EDS Panel 83	EDS Panel 84	EDS Panel 138
Before Dust Loading	92.15 (ΔR_s = 2.05%)	91.95 (ΔR_s = 2.25%)	92.05 (ΔR_s = 2.15%)
After Dust Loading	87.63	84	82.90
After EDS Activation	89.85 (ΔR_s = 2.2%)	88.1 (ΔR_s = 2.85%)	89.4 (ΔR_s = 2.65%)

Average Obscuration and clearance (%):

Panel	EDS Panel 83	EDS Panel 84	EDS Panel 138
Before Dust Loading	0.17	0.39	0.16
After Dust Loading	8.23	14.1	6.50
EDS Clearance	97.46	96.66	96.60

(DRE)			
Figure of Merit (FOM)	44.3	33.9	36.5
EDS Efficiency	0.90	0.88	0.89

The films were then tested using PEDOT:PSS electrodes (transparency > 90%). Specular reflectivity was measured both before and after removal of the deposited dust layer, as shown in Table 3. However, applying PEDOT: PSS or AgNW electrodes using screen printers could not allow electrode width smaller than about 75 μm. Using manual screen-printing, the average width was approximately 100 μm, and center-to-center spacing was 800 μm. Table 2 shows the specular reflectance and dust removal efficiency data for EDS mirrors using PEDOT:PSS electrodes with w = 100 μm and s = 900 μm. The table also shows the calculated values of the Figure of Merit (DRE/ ΔR_s) and the EDS efficiency (DRE × R_{se}). These results show that the FOM plays a greater role in determining the effects of electrode parameters and materials on EDS performance.

10. Specular Reflectivity Restoration by EDS Operation for Removing Deposited Dust from the Mirrors:

10.1 Silver nanowire ink electrode with Polymer (PET) film: Experimental data from a prototype EDS-mirror made with silver nanowire electrodes having the same geometry as the PEDOT:PSS EDS are shown in Table 3. Specular reflectivity after EDS integration was low, because the polymer film (PET) has a high absorption. Figure 17 shows the restoration of specular reflection efficiency of the EDS-mirror after 10 consecutive trials in which dust deposition was followed by EDS-activated removal.

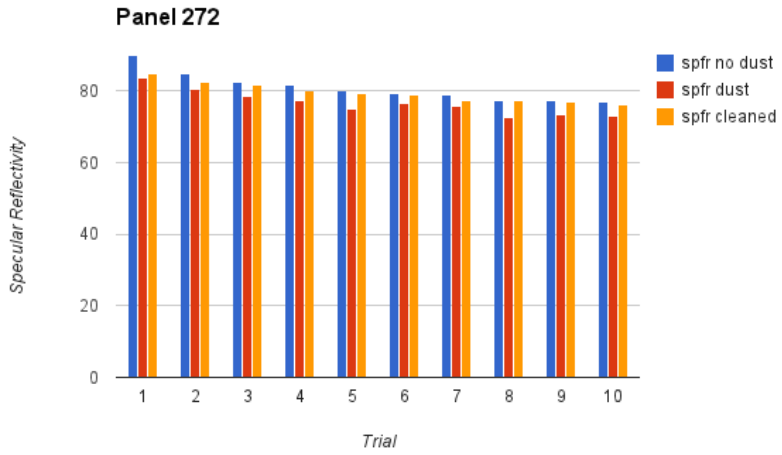

Figure 17 - Restoration of specular reflection efficiency of a prototype EDS constructed with AgNW electrodes (500 nm thickness, 75 μm width, 700 μm separation) encapsulated by a dielectric 100 μm-thick polymer (PET) film.

Since PET film has a high absorption coefficient (close to 10%), the initial reflection efficiency R_{se} was low. The blue bars in Figure 17 represent R_{se} before dust deposition; the red bars represent R_{se} after dust deposition; and the orange bars represent restored specular reflectance. These latter values are > 90% of the initial value.

10.2 Silver nanowire ink electrode with ultrathin flexible glass film: Figure 18 shows experimental data on restoration of specular reflectivity (SR) and percentage dust removal for an EDS-based mirror subjected to repeated dust deposition events within an environmental test chamber. The total mass of deposited dust represents more than a year of soiling in the Mojave Desert region.

In Fig. 18, the gray line represents loss of SR after additional dust was deposited on the mirror following EDS operation. The new dust layer caused additional ΔSR. The EDS was activated again to remove the newly deposited dust and to restore the mirror's SR. In each experimental run, dust was deposited until the loss ΔSR was approximately 3% to 5%, after which the EDS was operated again to maintain an SR close to 90%.

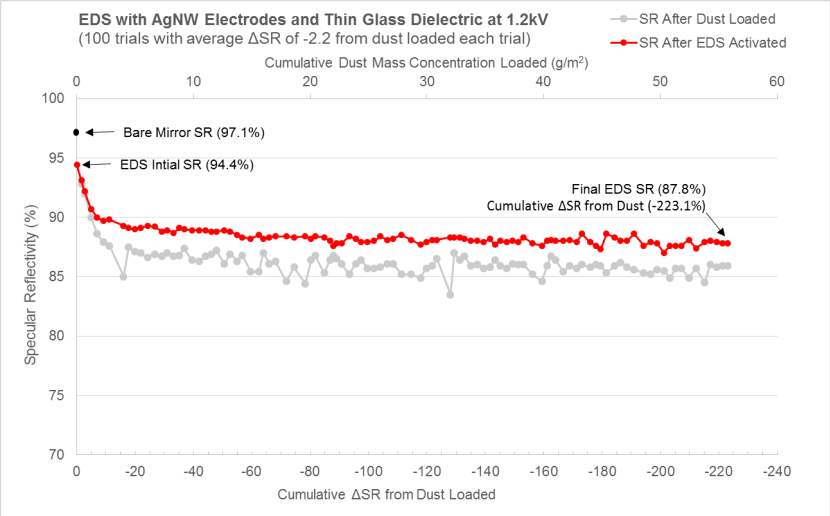

Figure 18 – Experimental data on restoration of specular reflection over 100 dust-deposition cycles. Original mirror SR was 97.1%. After EDS integration, SR was 94.4% without any dust. *Gray line:* Reduction in SR as surface dust is deposited. *Red line*: Restored SR after EDS activation for 1 min.

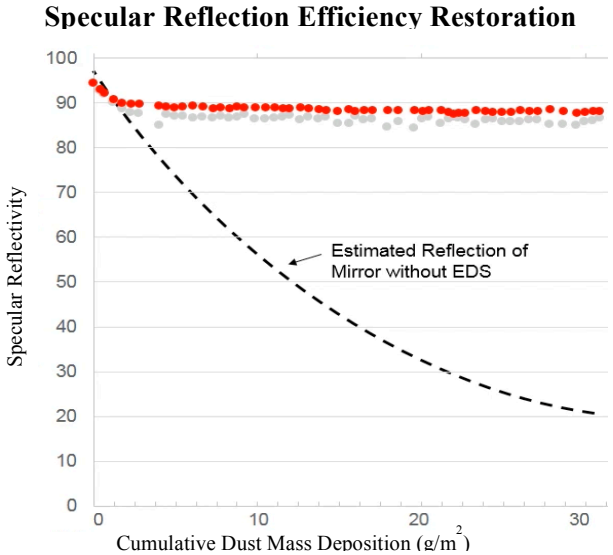

Figure. 19. Specular reflection efficiency as a function of cumulative surface mass density of dust in g/m^2.

The *x*- axis in Fig. 18 represents the cumulative ΔSR caused by repeated dust deposition. The experiment simulates a field condition wherein dust is deposited continuously on a CSP mirror, and the EDS is operated intermittently as needed for restoring SR.

Figure 19 shows that a transparent EDS film retrofitted on a mirror having an initial reflectance 97% would reduce the initial reflection efficiency by 3%, i.e., to 94%. After the EDS is laminated on the mirror, it would be able to maintain SR at a level above 87%. Without dust removal, the SR value would drop to less than 30% reflectance. This experiment was carried out in an environmental chamber. The results show that an EDS can maintain mirror specular reflectance at more than 90% of initial specular reflection efficiency. This mitigation of dust deposition is performed without requiring any water.

Modeling of EDS application in the Mojave Desert: The advantage of daily EDS cleaning, compared to water cleaning every 23 days (typical for CSP plant operations,) is evident in the simplified model of Fig. 20, which shows the variation in SR over 100 days. The graph assumes a constant average dust-deposition rate of 1.9 g/m^2 and a 3 to 30-µm particle-size distribution, as is generally found in the Mojave Desert, where dust deposition is about 30 g/m^2/yr. With daily EDS use, followed by water cleaning after 100 days (red), the average SR over 100 days is maintained at 95%. With water-based cleaning only, the average SR over 100 days falls to 75%. Much less water is required for the cleaning cycle that includes EDS operation, because water cleaning occurs every 100 days, rather than every 23 days.

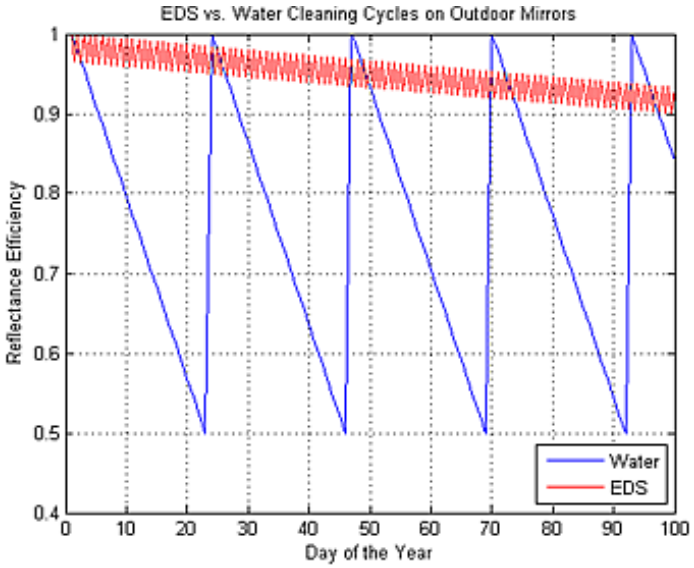

Figure 20 - Loss of specular reflection efficiency as a function of time, assuming constant soiling rate of 30 g/m^2/year. Water-based cleaning every 23 days is compared to daily EDS use and water cleaning after 100 days, average reflection efficiency for 100 days would be 95%. With water-based cleaning only, the average specular reflection will be 75%. EDS operation does not require any water.

11. Power Supply Design and Construction:

The power supply unit provides the voltage signals that drive the EDS electrodes. Each of its three output phases consist of a periodic square wave of 500 – 2 kV magnitude with an adjustable duty cycle that allows for a 10-25% voltage-activation overlap between adjacent electrodes.

Table 4. Performance Capabilities of Current and Future Power Supply Designs

Feature	**Gen**	**Gen 2**	**Gen 3**	**Gen 4 (in development)**
Controls MOSFETs without Driver	×	×	✓	✓
Adjustable Frequency	✓	✓	✓	✓
Adjustable Duty Cycle	×	✓	×	✓
Number of Processors	0	2	1	1
Variable Voltage Output	✓	✓	✓	✓
Maximum Operating Voltage	15V	12V	12V	12V
Maximum Output Voltage	1.2kV	1.2kV	2kV	2kV
Maximum Frequency	100Hz	10Hz	5Hz	100Hz
High-Voltage Shutoff Switch	×	✓	×	✓

Input controls allow the user to adjust the duty cycle (jumper wires), the frequency (DIP switches), and the voltage (potentiometer) of the output, to allow for testing along each of these parameters. A block diagram of the power supply is shown in Fig. 21. The features of the power supply design is shown in Table 4.

Currently, the second and third generations of the power supply are working exactly as designed. They are being used to drive the EDS with 1kV and 2kV, respectively, for testing at these different voltages. As shown by the table, the power supply design has been fine-tuned over time, towards: 1) less complex circuitry, by reducing the number of processors and the need for a MOSFET driver; 2) a better-controlled output, including variability in frequency, duty cycle, and voltage fine-tuning; 3) a lower operating voltage, down to 12V from the original 15V; and 4) a higher output voltage, from 1kV in previous generations to 2 kV in the newest ones, which has proven to be more effective in cleaning the panels.

A fourth generation is currently being prototyped, which combines the most useful features of each previous generation. The design outputs a 2kV square wave, while maintaining the frequency, duty cycle, and fine voltage variability of the previous versions. By using a more elegant circuitry, it eliminates the need for both a second processor, and a MOSFET driver IC. By the prototype's completion, it will be optimized in terms of power consumption.

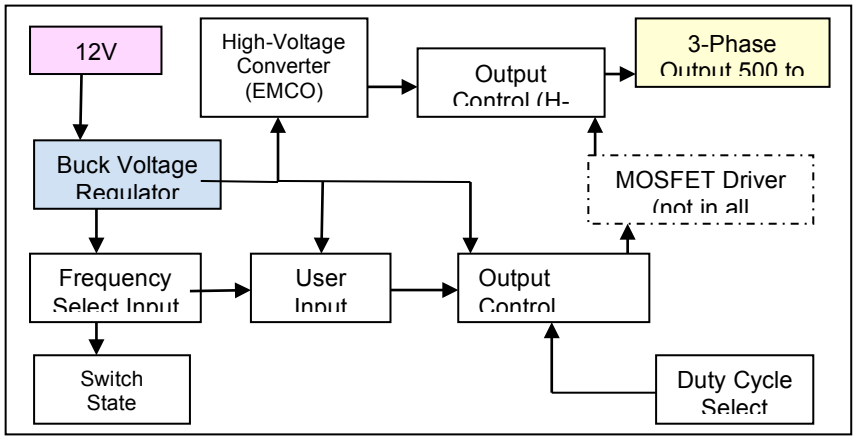

Figure 21 - Block diagram of power supply used for activating EDS electrodes with 3-phase voltages

11.1 Power Supply Safety Features

As with any high-voltage circuit, there are necessary safety considerations in using the EDS power supply. The component responsible for the high voltage output, the EMCO GP-12, is incapable of delivering more than about 1 milliamp of current, hence an accidental shock may hurt slightly but will not cause harm or injury.

In the 4th generation supply, a capacitor is used as a charge pump to increase the output voltage from the 1.2-kV EMCO component. Because capacitors store charge and can produce high current for short periods of time, basic precautions are taken – e.g., keeping the box closed during operation, and not touching the leads of the capacitor.

The electrodes of the EDS, as well as its interconnections, are encapsulated in high dielectric strength electrical insulation. Our objective is to meet all relevant IEEE safety standards regarding electrical systems as are applicable to solar power plants.

12. Field Testing at Sandia National Laboratories:

Six EDS mirrors and three control mirrors were shipped to SNL for field testing. Figure 22 shows the EDS mirrors (top) and the control mirrors (bottom) as installed at the SNL solar field. One goal of this testing was to examine how well the mirrors could withstand rain and early-season snowfalls, and if the Willow-glass construction succumbed to any water leakage.

The panels were cleaned and initial specular reflectance measurements were taken using a standard D&S specular reflectometer. The control mirrors were not cleaned. The specular reflection efficiency was measured once every week following EDS activation.

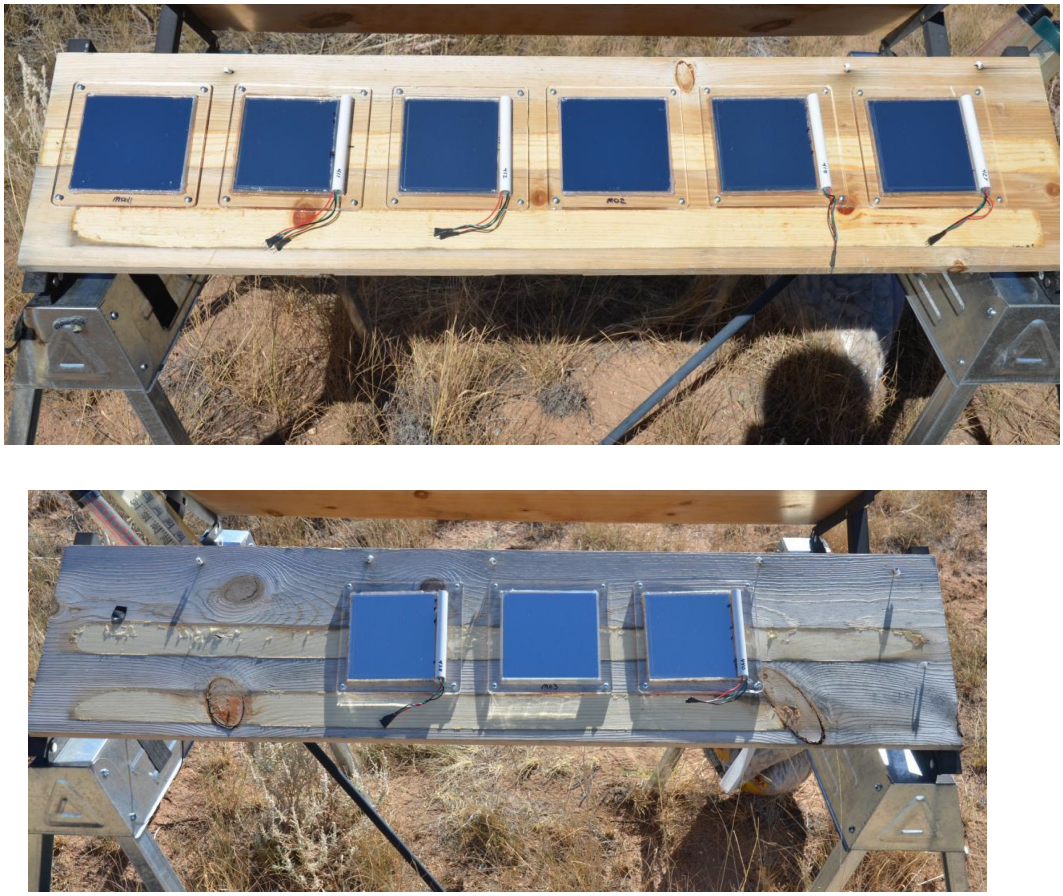

Figure 22 - Photograph of the six EDS (top row) and three control (non-EDS) mirrors in place for long-term testing at the SNL solar field

Table 5 shows initial measurements of specular reflection efficiency just after mirror installation, as well as the specular reflection efficiency measurements taken one week later. All mirrors show a reflectivity > 90%. More data over a longer period of time will likely yield a show consistent difference between control and EDS-mirror performance. Initial measurements were taken again in the field after the mirrors were mounted on the stands. Screws were used to mount the mirror samples.

Table 5. Reflectance Data on BU EDS Samples for Outdoor Testing at Sandia NSTTF – Second Field Test:

Date:	10/16/14	10/16/14	10/23/14
D&S	(in lab)	(in field)	

Calibration:			
before data coll	97.4	97.4	97.4
after data coll	97.4	97.4	97.4
Reference Mirror:			
before data coll	94.3	---	94.3
after data coll	---	94.2	94.3
Time (PM)	1:40 PM	2:40 PM	3:45 PM
T (°F)	---	77	74
RH (%)	---	21	25
Sample ID			
M01	95.7	95.7	93.6
AVG	**95.78**	**95.74**	**94.38**
STDEV	**0.08**	**0.11**	**0.52**
411	94.8	94.7	93.7
AVG	**94.78**	**94.70**	**93.76**
STDEV	**0.08**	**0.07**	**0.22**
412	94.5	94.4	93
AVG	**94.56**	**94.42**	**92.90**
STDEV	**0.05**	**0.04**	**0.82**
M02	95.6	95.5	94.4
(reference)	95.4	95	94.3
AVG	**95.36**	**95.16**	**94.26**
STDEV	**0.15**	**0.29**	**0.21**
418	93.7	93.6	92.7
AVG	**93.68**	**93.48**	**92.70**
STDEV	**0.31**	**0.36**	**0.16**
427	94.4	94.1	93.2
AVG	**94.34**	**94.22**	**93.40**
STDEV	**0.15**	**0.16**	**0.12**
438	93.5	92.8	92
AVG	**93.58**	**93.40**	**92.36**
STDEV	**0.29**	**0.34**	**0.22**
M03	95.5	95.1	94.6
(reference)	95.2	95.1	94.1
AVG	**95.40**	**95.34**	**94.34**
STDEV	**0.14**	**0.26**	**0.19**
440	92.1	91.8	91.9
AVG	**92.70**	**92.44**	**91.78**
STDEV	**0.41**	**0.51**	**0.24**

Note. Initial measurements were taken in the lab after the mirrors were cleaned with alcohol solution. Nine samples total (6 EDS mirrors, 3 reference mirrors)

12.1 Summary of field-testing results: First two weeks The EDS mirrors worked well under the outdoor conditions at the solar field. There was a heavy rainfall during the third week after installation and the EDS mirrors became nonfunctional. Water ingress inside the laminations was clearly visible. Several electrodes lines were not activated when retested in the lab. These failures were unexpected since we believed that the epoxy encapsulation should prevent water penetration. It appears that we need to use more effective encapsulation processes based on the research previously published on this subject. Several environmental aspects including temperature variations and exposures to water affecting the encapsulants cause the ingress of water [38 – 40].

12.2 Durability tests for AgNW electrodes: Silver nanowire (AgNW) electrodes are used extensively nowadays in the touch screen displays of portable devices such as smartphones, hybrid laptops, tablets, and flat-panel displays. The material is durable provided that the electrodes are hermitically sealed against moisture and oxygen penetration. Formulation of AgNW ink for screen-printing was synthesized in our laboratory, and we developed an annealing process for obtaining the desired conductivity and transparency. We are still researching the durability of AgNW ink for outdoor applications.

13. Prototype EDS mirror development by gravure offset printing with Ag-paste electrodes printed on willow glass at ITRI: In collaboration with Corning and ITRI, we performed preliminary evaluation of EDS mirror developed in a production environment at ITRI. Since commercially available AgNW-ink formulation for gravure offset printing is not yet available, we used silver paste ink for initial evaluation. The results are shown in Table 6.

Table 6. Specular reflectance efficiency of EDS mirrors with three different types of electrodes: AgNW (100/700), Ag-paste (50/700), and ITO (70/700) width/spacing ratio. The first column shows the specular reflectivity before EDS film lamination.

	Back mirror	AgNW	ITRI samples (silver paste)	ITO
	95.3	95.2	84.7	89.6
	95.3	94.7	87.2	91
	95.2	94.2	82.6	88.2
	95.3	94.5	88.8	90.7
	95.4	94.7	82.9	87.9
Average	95.3	94.66	85.24	89.48

These results agree well with the predicted values from optical modeling. Since these electrodes are printed in production environment, we believe that the yield rate and reliability would be much improved. Similarly, interconnections and encapsulation performed under production conditions would provide desirable outdoor performance.

From the optimization studies, we found that electrode width over the range 25 to 50 μm, with a center-to-center spacing of 700 to 800 μm, may provide EDS films with the best performance.

14. Economic Analysis: EDS Manufacturing & Operations Processes:

The goals for EDS cost modeling and allied economic analysis effort are twofold: to assess the economic viability of the EDS technology used in conjunction with solar collecting technologies when it is put in place into large scale EDS operations, and to help make informed development decisions as the EDS technology matures in the lab. This analysis is made up to two modules: (*i*) Manufacturing costs analysis, and (*ii*) Integrated cost analysis that incorporated both the manufacturing and operational costs.

Based on this integrated analysis, we propose a levelized cost of mirror cleaning (LCOMC) metric to link the EDS-enhanced reflectivity gains with the relevant product and installation costs, as well as with the direct and indirect costs associated with plant operation and maintenance. The LCOMC metric accounts for the fact that enhanced reflectivity owing to EDS technology allows the plant operators to specify a suitably smaller optical capacity plant in order to deliver a fixed power production target. We illustrate our proposal with a dataset on deluge cleaning of a scaled solar power plant configuration. For the configuration studied, it is shown that, if the EDS technology production and installation cost is $\$10/m^2$, then its LCOMC is 7.9% below the LCOMC for a comparable deluge cleaning alternative. Thus, the proposed LCOMC metric provides a methodology for systemic assessment of the economic impact of the EDS technology (and other mirror cleaning technologies), early in its technology development cycle. This integrated analysis has been published [41 - 44].

14.1 Manufacturing Cost Analysis: Process Based Cost Modeling was developed as a method to understand the economic implications of bringing a technology to the market. It captures the engineering approaches to avoid expensive strategic errors in product development and deployment, early in the technology development cycle [2, 3]. Modeling the EDS as a developing technology required a set of initial assumptions. That is, user inputs for the EDS manufacturing cost module are centered around design assumptions based on the multi-layer

screen-printing electrode deposition. There are four different categories of user inputs in the EDS manufacturing module: EDS Design, Exogenous Data, Process Inputs, and Material Characteristics. In all, there are over 100 user inputs. A few examples of these inputs are displayed in a user-friendly format and coded in yellow. An example of these inputs can be seen in Table 7.

Table 7. Example of EDS Manufacturing Process Inputs

EDS DESIGN		
Substrate Width	15	cm
Substrate Length	15	cm
Substrate Thickness	0.5	cm
Electrode Width	100	µm
Electrode Length	12	cm
Electrode Thickness	50	µm
Number of Electrodes	130	

The process inputs for the EDS manufacturing module were carried out in two stages based on the two separate design configurations shown in Figure 23. The initial analysis corresponds with the configurations involving Silver EDS Screen-print and PEDOT EDS screen prints corresponding to the fabrication process flow of the three-phase multi-layer EDS shown on the left hand side of Figure 23. (Please see reference 4 for details of the initial analysis with cycle time set at 23 minutes.) Revised analyses consider modified process steps shown on the right hand side of Figure 24.

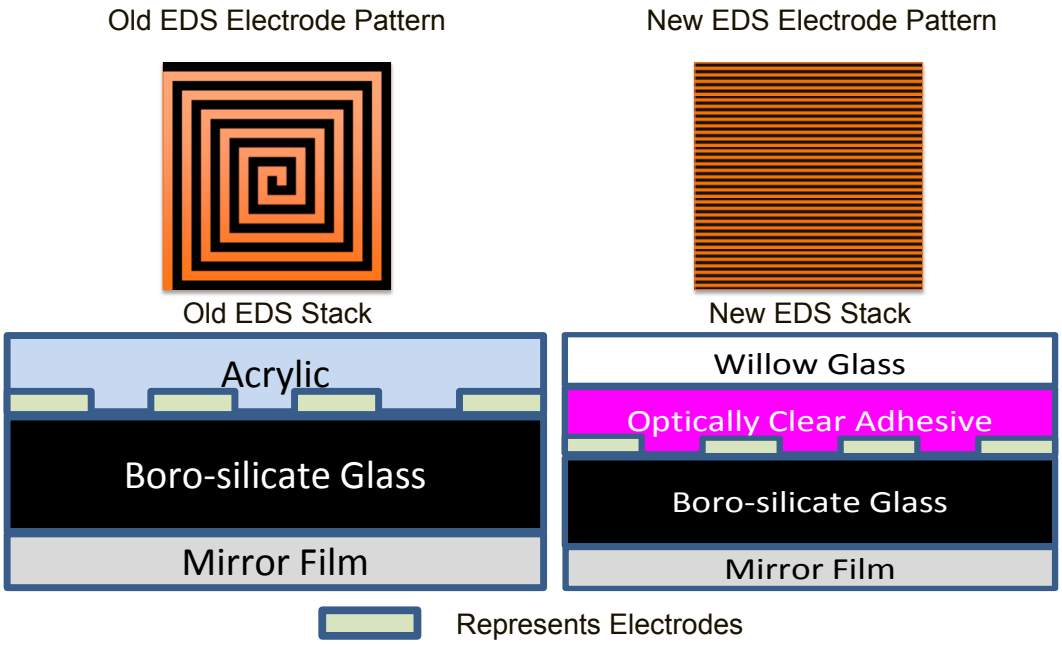

Figure 23: Initial (left) vs. revised (right) EDS electrode pattern and stack

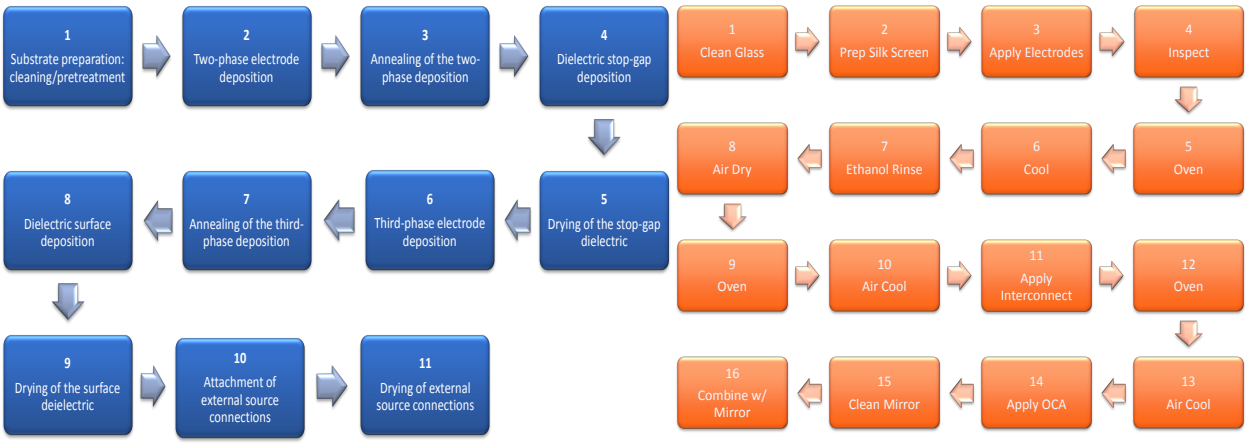

Figure 24: Initial process flow (left) & revised process flow (right)

Based on these analyses, we can identify two key figures of merit (**unit cost** and **break even time**) and a set of life cycle and scalability considerations as key determinants of the economic feasibility of our EDS solution. For the initial design and a manual cleaning process, our analysis indicates that the cost of the pilot module was about $25, as is shown cases 1 and 2 in Table 8. This analysis does not consider the power supply costs, which were excluded for brevity.) With a new design configuration ("Silver Willlow Screen Print"), this cost is shown to be about $27.13. This result does not include the material cost of the Willow glass, and these data do not include production scale-up analysis. Analysis of full-scale design, with larger volumes, will

require additional work and data from suppliers. This task has deferred to the next stage of the project.

Table 8: Lab Scale Manufacturing Cost

Case #	Size	Process Configuration	Volume	Unit Cost ($)	Break Even Time (Years)
1	15 x 15 cm	Silver EDS Screenprint	1000	25.50	NA
2	15 x 15 cm	PEDOT EDS Screenprint	1000	25.33	NA
3	15 x 15 cm	Silver Willow Screenprint	1000	27.13	NA

14.2 Integrated Cost Analysis Using LCOMC Metric:

The levelized cost of mirror cleaning (LCOMC) is a metric that we have developed as part of this project to account for manufacturing as well as operating costs over the entire life cycle of a solar plant. In order to put everything on equal terms, we divide our upfront construction costs by the expected life of the plant, thus causing them to become amortized costs. We define the LCOMC as:

LCOMC = CAnnual / ESR (in $/KWh)

Where CAnnual is the annualized cost associated with installation, operation, and maintenance of mirror cleaning technologies, including costs associated with the mirrors themselves. ESR is the expected annual average power delivered (in KWh/year). This latter term will account for annualized loss of reflectivity associated with either deluge cleaning or by the integration of EDS on the mirrors. Because the current R&D effort on EDS is focused on demonstration of technology readiness, the manufacturing costs described in Table 8 account for lab-scale production only. We anticipate that detailed manufacturing readiness (MR) studies, including scaling up of production volume using automated processes, will be conducted subsequently. Thus, the projected costs for the technology is likely to come down significantly. Based on current projections of material and design alternatives listed in Table 3, we explore values ranging from $5 to $30 per m^2 for the production and installation cost scenarios. These cost scenarios have been estimated following a process-based cost analysis study of the design parameters. The initial goal, based on operating practice at Abengoa Solar, is to complement the EDS technology with a substantially reduced (roughly 25% of the full cleaning schedule) water-based cleaning plan. These reduced water costs are also reflected in our analysis of the levelized costs.

Table 9. Candidate EDS Electrode Materials And Geometries

Parameter	**Values**
Materials	Ag nano-wire ink (AgNW Ink), AZO, ITO, PEDOT

Widths (μm)	50, 75, 100
Heights (μm)	0.25, 0.5, 0.75, 1
Inter-electrode spacings (μm)	300, 500, 750, 1000, 2000

14.3 Baseline LCOMC (with Deluge Cleaning):

We establish a baseline by computing the LCOMC with a full schedule of deluge cleaning first. This schedule reflects current the operating practices at Abengoa Solar. To stay consistent with the levelized cost methodology, we assume the discount rate to be 0% (this assumption can be relaxed). We have set up these costs such that they scale based upon a "Soiling Factor" (ratio of actual mirror reflectance to initial clean reflectance). Relevant costs are lumped into 3 groups: (1) Pump Costs, (2) Indirect Costs, and (3) Deluge Cleaning Costs including a) Water & detergents, b) Labor, and c) Equipment

14.4 LCOMC with EDS:

We account for the following annualized costs in various EDS cost scenarios. Our methodology for integrating EDS works by applying changes directly to the base case numbers described this Section. The primary driver for our savings is that we institute an improved Soiling Factor (therefore flowing through the model and reducing various parameters dependent on the soiling factor). It should be noted that we are still amortizing all upfront costs over the life of the plant as described previously. Relevant costs are lumped into:

1. Initial EDS installation amortized over the estimated life of the power plant. These costs account for the marginal cost reduction of fewer (or marginal cost of additional) loops of mirrors to yield baseline energy production.
2. Replacement costs of a EDS mirrors per year owing to lifecycle losses.
3. Operations & maintenance costs per year of EDS.
4. In addition, we assume that that the EDS system is implemented to work with a reduced deluge cleaning schedule. The margin cost reduction of lower (or marginal cost of more) deluge cleaning to maintain a specific average specular reflectivity is included.

14.5 Results

Data from the configurations described above were used to run a series of Monte Carlo simulations (n =1000) in each test scenario: the base case, and EDS with unit cost set at \$5, \$10, \$20 and \$30 per m^2. The computed, cumulative distribution functions (CDFs) are then normalized with respect to LCOMC of deluge cleaning. These yielded five normalized CDFs, as shown in Figure 25. Corresponding summary statistics for the percentage reduction (gain) in the expected values of LCOMC for the four EDS cost scenarios are shown in Table 10. We have also conducted related sensitivity analysis for issues such variation in labor and water costs.

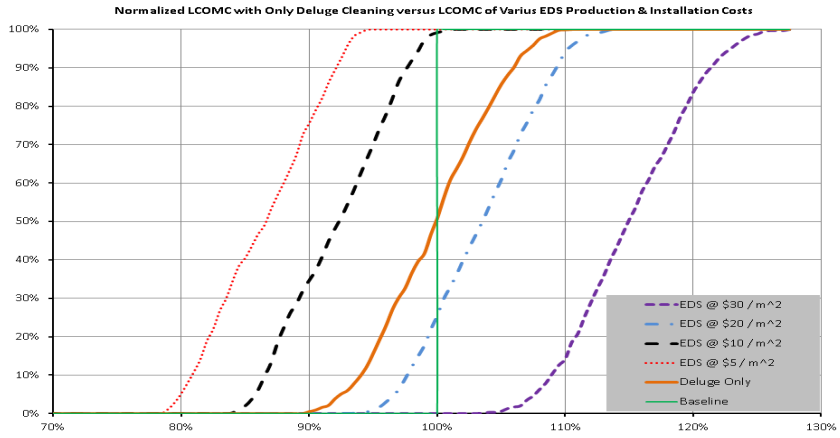

Figure 25. CDFs of Levelized Cost of Mirror Cleaning in Five Scenarios

Table 10. EDS LCOMC Summary Statistics Normalized with Respect to Deluge Cleaning LCOMC

Scenario	EDS @ $5 / M^2	EDS @ $10 / M^2	EDS @ $20 / M^2	EDS @ $30 / M^2
% Change in Expected LCOMC	-13.6%	-7.9%	3.4%	15.0%

14.6 Roadmap

In summary, for the scenarios examined in this study, the economic viability of EDS technology is predicated upon the upfront production and installation costs. If these technology costs could be brought down to $10/m^2, then there would be a 7.9% reduction in the percentage change for the expected value of LCOMC, when compared with a deluge cleaning solution. This reduction can be further increased to 13.6% if the cost is reduced to about $5/m^2. Conversely, EDS technology is not likely to be economically viable if the cost stays at $20/m^2 or more.

Two major limitations of the current work are: (*i*) analysis is predicated on lab scale data (TRL 3); and (*ii*) lack of access to key supplier data on unit costs for full scale production. We are proposing follow-on work to explore the scale up of the design to 50 cm × 50 cm and 100 cm × 100 cm units. We also propose to collect data on volume production and, in so doing, plan to study the commercialization potential at TRL6. We anticipate that such a scale-up effort will reveal opportunities for the usage of alternative technologies, optimization of process parameters, and allied learning opportunities to reduce the LCOMC.

CONCLUSIONS

List of Completed Project Goals:

1. Established the proof-of-concept of the application of transparent electrodynamic screen (EDS) for self-cleaning concentrating solar power (CSP) mirrors.

2. Developed EDS-integrated solar mirror as a team effort between BU, Abengoa Solar, and Sandia National Lab to demonstrate self-cleaning operation of CSP mirrors in semi-arid atmospheres without requiring water or manual labor.

3. Fabricated lab-scale (15 cm x 15 cm) prototype EDS-integrated mirrors for both flat and curved surfaces. Demonstrated self-cleaning properties of CSP mirrors with EDS integration with 90% dust removal efficiency.

4. Completed lab and initial field-testing with prototype EDS-integrated mirrors with flat and curved surfaces and on silvered polymer reflectors for their applications to parabolic troughs and heliostats.

5. Developed flexible transparent EDS film for retrofitting applications to CSP mirrors. Evaluated performance of film-based EDS for their retrofitting applications to solar mirrors.

6. Optimized EDS electrode geometry and materials and establish durability of the EDS-incorporated CSP mirrors.

7. Analyzed EDS performance under simulated and actual outdoor conditions (optical radiation, impact resistance, scratch resistance, exposure to detergents and other chemicals) with bench-scale tests at BU.

8. Conducted an industry-validated cost/benefit analysis showing a reduction in the amortized cost (e.g. capital + O&M costs) of the solar field over a 30-year lifetime for an EDS-integrated solar mirrors as compared to a baseline water-based cleaning systems. Applied a well-established and appropriate analysis process in collaboration with Abengoa Solar.

9. Demonstrated EDS application showing:

- Average dust removal efficiency ≥ 90%/cleaning cycle over a wide range of dust loading on the test EDS surface
- Average energy requirement ≤ 3 Wh/m^2/cleaning cycle
- Average loss in reflectivity ≤ 1% compared to non-EDS clean mirrors
- Average gain in reflectivity of the EDS surface ≥ 5% higher as compared to a non-EDS surface
- Methods of successful encapsulation process against moisture and oxygen penetration under outdoor conditions cold not be accomplished.

10. The economic viability of EDS technology is predicated upon the upfront production and installation costs. If these costs could be brought down to \$10/m^2, then there would be a 7.9%

reduction in the percentage change for the expected value of LCOMC, when compared with a deluge cleaning solution.

PATH FPRWARD

Technical roadmap established for manufacturing and field-evaluation

Based on our success in accomplishing the goals of the DOE CSP 5794 project, we have submitted proposal FOA 0001186-1599 under the CSP APOLLO Program to develop an advanced operation and maintenance method based on EDS mirror cleaning, reduce the O&M cost of CSP power plants, improve efficiency and reliability of CSP mirror performance, and conserve water.

We envision the maintenance of high mirror reflection efficiency by maintaining clean optical surfaces without water or manual labor will benefit the CSP industry and enable a potential multi-GW capacity without creating an unsustainable demand the fresh water needed for mirror cleaning.

The proposed studies will be performed in three phases over a period of three years in collaboration with Sandia National Labs, BrightSource Energy, Corning Inc., Industrial Technology Research Institute (ITRI), Oak Ridge national Laboratory and Geodrill Company. We established a prototype EDS mirror manufacturing process in collaboration with Industrial Partners and National Laboratories (SNL and ORNL)

1. BrightSource: We are collaborating with **BrightSource Energy** for field-evaluation of EDS mirrors, quality assurance tests in applying EDS to heliostats, and field-evaluation of EDS-mirror prototypes. These tests will be performed at the Ivanpah plant in the Mojave Desert, and at Dimona plant in southern Israel..

2. Geodrill Company: Geodrill Company is involved in cleaning mirrors in CSP plants and solar panels in PV plants in the Atacama Desert region in Chile. This remote area has the highest direct normal irradiance in the world, but availability of water and labor is severely limited. Their representatives visited our laboratory and are working to have a NDA with BU for collaboration.

3. Corning: Over the past year, we have been working with Willow Glass™ made by Corning to produce EDS-based mirrors. These have shown superior performance with respect to (1) highest specular reflectivity, (2) mechanical flexibility, (3) resistance to UV radiation, scratches, and impact, (4) excellent surface smoothness, and (5) adhesion of the electrodes. This product is projected by Corning to have an outdoor durability of 25+ years. To date, Corning has been supplying us with samples of Willow Glass at no cost.

4. Industrial Technology Research Institute (ITRI): ITRI is contributing to the project by producing several prototype EDS using Gravure Offset Printing (GOP) process. They have produces 8 prototype EDS for preliminary feasibility studies. We have tested the prototype EDS with silver paste electrodes and the results are promising. The GOP based EDS prototypes were produced in production environment since the process is compatible for low-cost roll-to-roll production.

5. Sandia National Laboratories: We have collaborated with SNL in the optical modeling of different geometrical configurations of EDS electrode assemblies, leading to the optimization of high specular reflection efficiency and dust removal capabilities. SNL helped us in the field-testing of EDS samples. We also worked with SNL in modeling LCOMC and LCOC for a comparative study between water-based versus EDS-based mirror cleaning.

6. ORNL: We plan to work with the Oak Ridge National Laboratory to investigate the use of hydrophobic and super-hydrophobic coatings added to the outer EDS surface. While EDS is an active method for cleaning solar mirrors, requiring no water or mechanical wiping, it works best under dry conditions. The addition of a passive superhydrophobic coating (SHC), which reduces dust adhesion, will enhance performance of the EDS and expand its range of operation to high RH levels. Dust removal via EDS can aid outdoor durability of the nanostructure and would thus provide a synergistic approach for high dust-removal efficiency under both wet and dry conditions.

REFERENCES

1. Kurokawa, K, et al. [Energy from the Deserts], ISBN 978-1-84407-4, Earth Scan, London, UK (2007),

2. Sarver, T., Al-Qaraghuli, A., and Kazmerski, L. L., "A comprehensive review of the impact of dust on the use of solar energy: History, investigations, results, literature, and mitigation approaches,". *Renewable and Sustainable Energy Reviews, 22*, pp. 698–733, (2013),

3. Sayyah, A., Horenstein, M. N., and Mazumder, M. K., 2013. "Energy Yield Loss Caused by Dust Deposition on Photovoltaic Panels," Solar Energy (2014),

4. Reheis, M. C. and Kihll, R., "Dust deposition in southern Nevada and California, 1984 – 1989, Relations to climate, source area and source lithology," Journal of Geophysical Research, Atmospheres, 100, D5, pp8893 – 8918, May (1995),

5. Aguado, E., "Effect of advected pollutants on solar radiation attenuation: Mojave Desert," Atmospheric Environment. Part B. Urban Atmosphere Volume 24, Issue 1 Pages 153-157 (1990).

6. Edward Fuentealba, Pablo Ferrada Francisco Araya, Aitor Marzo, Cristóbal Parrado, Carlos Portillo, "Photovoltaic performance and LCOE comparison at the coastal zone of the Atacama Desert, Chile" Energy Conversion and Management, Energy Conversion and Management 95 (2015) 181–186

7. Appels, R., Muthirayan, B., Beerten, A., Paesen, R., Driesen, J., Poortmans, J., 2012. The effect of dust deposition on photovoltaic modules. In: 38th IEEE Photovoltaic Specialists Conference (PVSC), 3–8 June. Austin, TX, pp. 001886–001889.

8. Brown, K., Narum, T., Jing, N., 2012. Soiling test methods and their use in predicting performance of photovoltaic modules in soiling environments. In: 38th IEEE Photovoltaic Specialists Conference (PVSC), 3–8 June. Austin, TX, pp. 001881–001885.

9. Piliougine, M., Cańete, C., Moreno, R., Carretero, J., Hirose, J., Ogawa, S., Sidrach-de-Cardona, M., 2013. Comparative analysis of energy produced by photovoltaic modules with anti-soiling coated surface in arid climates. Appl. Energy 112, 626–634

10. Scott R. Hunter, D. Barton Smith, Georgios Polizos, Daniel A. Schaeffer, Dominic FLee, Panos G. Datskos, "High and Low Concentrator Systems for Solar Energy Applications IX", edited by Adam P. Plesniak, Candace Pfefferkorn, Proc. of SPIE Vol. 9175, 91750J · © 2014 SPIE · CCC code: 0277-786X/14/$18 · doi: 10.1117/12.2061845 Proc. of SPIE Vol. 9175 91750J-1

11. Kochan, A., 2005. Robot cleans glass roof of Louvre pyramid. Indust. Rob.: An Int. J. 32 (5), 380–382.

12. Anderson, M., Grandy, A., Hastie, J., Sweezey, A., Ranky, R., Mavroidis, C., 2009. Robotic device for cleaning photovoltaic panel arrays. In: 12th International Conference on Climbing and Walking Robots and the Support Technologies for Mobile Machines, 9–11 September. Istanbul, Turkey, pp. 1–11

13. Mani, Monto., Pillai, Rohit., 2010. Impact of dust on solar photovoltaic (PV) performance: research status, challenges and recommendations. Renew. Sustain. Energy Rev. 14, 3124–3131

14. Masuda, S., K. Fujibayashi, K. Ishida, and H. Inaba, "Confinement and transportation of charged aerosol clouds via electric curtain," *Elect. Eng.Jpn.*, vol. 92, no. 1, pp. 43–52, (1972),

15. Mazumder, M. K., Horenstein, M., Stark, J. W., Girouard, P., Sumner, R., Henderson, B.,

Sadder, O., Hidetaka, I., Biris, A., and Sharma, R., "Characterization of electrodynamic screen performance for dust removal from solar pan- els and solar hydrogen generators," *Industry Applications, IEEE Transactions on, 49*(4), July, pp. 1793–1800, (2013),

16. Horenstein, M. N., Mazumder, M. K., and Sumner Jr, R. C.,. "Predicting particle trajectories on an electrodynamic screen–theory and experiment," *Journal of Electrostatics, 71*(3), pp. 185–188 (2013),

17. Jeremy W. Stark, Julius Yellowhair, John N. Hudelson, Mark Horenstein, and Malay Mazumder, "Optical Modeling of Reflectivity Loss Caused by Dust Deposition on CSP Mirrors and Restoration of Energy Yield by Electrodynamic Dust Removal", Proceedings of the 8th International Conference on Energy Sustainability and Fuel Cell Science, 2014,

18. John Hudelson, Jeremy Stark, Fang Hao, Zhongkai Xu, Hannah Gibson, Mark Horenstein, and Malay Mazumder, "Development and Evaluation of Prototype Transparent Electrodynamic Screen (EDS) integrated Solar Collectors for Automated Dust Removal", Proceedings of the 8th International Conference on Energy Sustainability and Fuel Cell Science, 2014

19. Arash Sayyah, Mark Horenstein and Malay Mazumder, "Optimization of Electrodynamic Screens for Efficient Removal of Dust Particles", Proceedings of the 8th International Conference on Energy Sustainability and Fuel Cell Science, 2014,

20. M. K. Mazumder, M. N. Horenstein, Jeremy Stark, John Hudelson, Arash Sayyah[1], Nitin Joglekar, Julius Yellowhair, and Adam Botts, "Self-Cleaning Solar Mirrors using Electrodynamic Dust Shield: Prospects and Progress", Proceedings of the 8th International Conference on Energy Sustainability and Fuel Cell Science, 2014,

21. A. Sayyah, M. N. Horenstein, and M. K. Mazumder, "Mitigation of soiling losses in concentrating solar collectors," in Photovoltaic Specialists Conference (PVSC), 2013 IEEE 39th, Tampa, FL, June 2013, pp. 0480–0485.

22. Lovegrove, K., and Stein, W., Concentrating Solar Power: Principles, Developments and Applications, Woodhead Publishing: Series in Energy, (2012),

23. Pettit, R. B; "Characterization of the Reflected Beam Profile of Solar Mirror Materials,"; Solar Energy Vol. 19: p. 733, (1977),

24. Short, W. D., "Optical Goals for Polymeric Film Reflectors"; National Renewable Energy Laboratory Report, (1988),

25. Al-Hasan, Ahmed Y., "A new correlation of direct beam solar radiation received by photovoltaic panel with sand dust accumulated on its surface", Solar energy, 63.5 (1998);

323 – 3335

26. D, C. Miller, M. D. Kem[e, C. E. Kennedy, and S. R. Kurz, "analysis of transmitted optical spectrum enabling accelerated testing of multi-junction CPV designs" Opt. Eng. 50 (1), 2010, 013003

27. W. C. Hinds, "Aerosol technology: properties, behavior, and measurements of airborne particles, 2n Edition, NY, Wiley, 1999.

28. [9]. Bohren C. F. and D. R. Huffman, [Absorption and Scattering of Light by Small Particles], John Wiley & Sons, New. York, (1983),

29. R. S. Berg, "Heliostat dust buildup and cleaning studies" SAND 78 – 0510. 1978, pp 1 – 34.

30. J. B. Blackmon and M. Curcija, Heliostat reflectivity variations due to dust buildup under desert conditions, Proc. Inst. Environ. Sci., 1978 169 - 183.

31. Arash Sayyah, Mark N. Horenstein, and Malay K. Mazumder, "A comprehensive analysis of electric field distribution in an electrodynamic screen." submitted to the Journal of Electrostatics on Dec 26, 2014.

32. Arash Sayyah, Mark N. Horenstein, and Malay K. Mazumder, "The electrodynamic screen: closed-form solutions for the electric field and dielectrophoretic forces," in Proceedings of the 2014 ESA Annual Meeting on Electrostatics, Notre Dame, IN, Jun. 17-19, 2014

33. Arash Sayyah, Mark N. Horenstein, and Malay K. Mazumder, "Analysis of electric field distribution and dielectrophoretic forces in an electrodynamic screen." to be submitted to Journal of Electrostatics.

34. Malay Mazumder, Mark Horenstein, Jeremy Stark, Atri Roychowdhury, Arash Sayyah and Hannah Gibson, "Electrostatic charging mechanisms for dust layer deposited on the surface of Electrodynamic Screen (EDS): Relevance to Self-Cleaning Solar Collectors", Presented at the 2014 Annual Meeting of the Electrostatics Society of America, June 17 – 19, 2014

35. Malay Mazumder[1], Mark Horenstein[1], Jeremy Stark[1], Julius Yellowhair[2], John Hudelson[1], Calvin Heiling[1], and Arash Sayyah[1]Electrodynamic Removal of Dust from Solar Mirrors and Its applications in Concentrated solar power (CSP) Plants, Presented at

the IEEE Conference at Van Cuvier, CA, Oct. 4 to 7, 2014; submitted for publication in IEEE-IAS Transaction

36. M. Radmilovi´c-Radjenovi´c, J.K. Lee, F. Iza, and G.Y. Park. "Particle-in-cell simulation of gas breakdown in microgaps". J. Phys. D: Appl. Phys., 38(6):950–954, 2005

37. Atten, P., H. Long Pang, and Jean-Luc Reboud, "Study of Dust Removal by Standing-Wave Electric Curtain for Application to Solar Cells on Mars," IEEE Transactions on Industry Applications, Vol. 45, No. 1, January/February (2009).

38. Czanderna, A. W., and Pern, F. G., 1996, "Encapsulation of PV modules using ethylene vinyl acetate copolymer as a pottant: A critical review, Solar Energy Materials and Solar Cells, vol, 43, pp. 101 -181,

39. King, D. L. et. al, 2000, "Photovoltaic module performance and durability following long-term field exposures", Progress in Photovoltaics: Research and Applications, Vol. 8, pp. 241 – 246

40. Ecofys, B. V., 2004, "Technology fundamentals: PV Module Manufacturing", Renewable Energy World, May-June Issue, Planning and Installation of Photovoltaic Systems, James and James (Ed), Earthscan, London, UK

41. Joglekar, N., E. Guzelsu, M. Mazumder, A. Botts, C. Ho (2014). A Levelized Cost Metric for EDS-Based Cleaning of Mirrors in CSP Power Plants. ASME - 8 th International Conference on Energy Sustainability, Boston, MA.

42. Field, F., R. Kirchain, R. Roth (2007). Process cost modeling: Strategic engineering and economic evaluation of materials technologies. JOM: Journal of Mineralogy, vol. 59, no. 10, pp. 21–32.

43. Fuchs, E. R. H., E. J. Bruce, R. J. Ram, and R. E. Kirchain (2006). Process-based cost modeling of photonics manufacture: the cost competitiveness of monolithic integration of a 1550-nm DFB laser and an electroabsorptive modulator on an InP platform. Journal of Lightwave Technology, vol. 24, no. 8, pp. 3175–3186.

44. Erickson, D.S. (2013). Fabrication and Cost Analsysis of Screen-Printed Electrodynmaic Shields for Solar Applications. Master of Sceince Thesis, B.U. College of Engineering.